

# A *Posteriori* Hyperspectral Anomaly Detection for Unlabeled Classification

Yulei Wang, Li-Chien Lee, Bai Xue, *Student Member, IEEE*, Lin Wang, Meiping Song,  
Chunyan Yu, *Member, IEEE*, Sen Li, and Chein-I Chang<sup>✉</sup>, *Life Fellow, IEEE*

**Abstract**—Anomaly detection (AD) generally finds targets that are spectrally distinct from their surrounding neighborhoods but cannot discriminate its detected targets one from another. It cannot even perform classification because there is no prior knowledge about the data. This paper presents a new approach to AD, to be called *a posteriori* AD for unlabeled anomaly classification where *a posteriori* indicates that information obtained directly from processing data is used as new information for subsequent data processing. In particular, *a posteriori* AD uses a Gaussian filter to capture spatial correlation of detected anomalies as *a posteriori* information which is included as new information for further AD. In doing so, *a posteriori* AD develops an iterative version of AD, referred to as iterative anomaly detection (IAD), which implements AD by feeding back Gaussian-filtered AD maps in an iterative manner. It then uses an unsupervised target detection algorithm to identify spectrally distinct anomalies that can be used to specify particular anomaly classes. To terminate IAD, an automatic stopping rule is also

Manuscript received August 24, 2017; revised November 17, 2017; accepted December 28, 2017. Date of publication March 14, 2018; date of current version May 21, 2018. The work of Y. Wang was supported in part by the Fundamental Research Funds for the Central Universities under Grant 3132017080 and in part by the Open Research Fund of Key Laboratory of Spectral Imaging Technology, Chinese Academy of Sciences under Grant LSIT201707D. The work of L. Wang was supported by the Fundamental Research Funds for Central Universities under Grant JB150508. The work of M. Song was supported by the National Natural Science Foundation of China under Grant 61601077. The work of C. Yu was supported by the National Nature Science Foundation of Liaoning Province (20170540095). (Corresponding author: Meiping Song.)

Y. Wang is with the Center of Hyperspectral Imaging in Remote Sensing in Information and Technology College, Dalian Maritime University, Dalian 116026, China, also with the Key Laboratory of Spectral Imaging Technology of Chinese Academy of Sciences, Xi'an 710000, China, and also with the State Key Laboratory of Integrated Services Networks, Xi'an 710000, China (e-mail: wangyulei@dlmu.edu.cn).

L.-C. Lee and B. Xue are with the Department of Computer Science and Electrical Engineering, University of Maryland Baltimore County, Baltimore, MD 21250 USA (e-mail: lcl7722@gmail.com; baixue1@umbc.edu).

L. Wang is with the School of Physics and Optoelectronic Engineering, Xidian University, Xi'an 710126, China (e-mail: lwang@mail.xidian.edu.cn).

M. Song is with the Center of Hyperspectral Imaging in Remote Sensing in Information and Technology College, Dalian Maritime University, Dalian 116026, China, and also with the State Key Laboratory of Integrated Services Networks, Xi'an 710000, China (e-mail: smping@163.com).

C. Yu and S. Li are with the Center of Hyperspectral Imaging in Remote Sensing in Information and Technology College, Dalian Maritime University, Dalian 116026, China (e-mail: 36202986@qq.com; listen@dlmu.edu.cn).

C.-I Chang is with the Department of Computer Science and Information Engineering, National Yunlin University of Science and Technology, Douliu 640, Taiwan, also with the Department of Computer Science and Information Management, Providence University, Taichung 09212, Taiwan, also with the Center of Hyperspectral Imaging in Remote Sensing in Information and Technology College, Dalian Maritime University, Dalian 116026, China, and also with the Remote Sensing Signal and Image Processing Laboratory, Department of Computer Science and Electrical Engineering, University of Maryland Baltimore County, Baltimore, MD 21250 USA (e-mail: cchang@umbc.edu).

Color versions of one or more of the figures in this paper are available online at <http://ieeexplore.ieee.org>.

Digital Object Identifier 10.1109/TGRS.2018.2790583

derived. Finally, it uses identified distinct anomalies as desired target signatures to implement constrained energy minimization (CEM) to classify all detected anomalies into unlabeled classes. The experimental results show that *a posteriori* AD is indeed very effective in unlabeled anomaly classification.

**Index Terms**—*A posteriori* anomaly detection (AD), anomaly discrimination, automatic target generation process (ATGP), constrained energy minimization (CEM), iterative AD (IAD), K-AD, Otsu's method, R-AD, unlabeled anomaly classification (UAC).

## I. INTRODUCTION

**A**NOMALY detection (AD) has received considerable interest in recent years due to advances of hyperspectral imaging technology which enables to uncover many unknown subtle targets that cannot be inspected visually or detected by prior knowledge [1]. One of the early approaches was developed by Reed and Yu [2], referred to RX detector (RXD). Since then, many techniques have been developed [3]–[37]. However, due to unavailability of prior knowledge, several challenging issues remain unresolved and need to be addressed for AD. First of all, what types of targets can be considered as anomalies? This issue was discussed in detail for anomaly characterization in [16] and [37]. Another issue is how to discern among anomalies once targets are declared to be anomalies. One solution was developed in [37] and [38] where a particular unsupervised target detection, called automatic target generation process (ATGP) developed in [10], was implemented in conjunction with AD to discriminate detected anomalies one from another. However, according to [39, Ch. 18], the presence of anomalies is closely related to spatial correlation of anomalies with their surrounding pixels. The anomaly categorization developed in [37] and [38] was pixel-based and did not take into account such surrounding spatial correlation. This paper extends the work in [37] and [38] to an approach, to be called *a posteriori* AD for unlabeled anomaly classification (UAC). The term of *a posteriori* is used to reflect the fact that the information used by *a posteriori* AD is obtained directly from processing data (i.e., after observing the data) as opposed to the commonly used AD which can be considered as *a priori* AD that only uses the original data sample information including windows to perform AD. *A posteriori* AD explores spatial information among detected anomalies as *a posteriori* information which is further used as new information to perform UAC without any prior knowledge, specifically, no need of knowing how many classes into which anomalies should be classified. Due to the fact that no prior knowledge can be used to label classes, the classes produced by UAC are unknown and, thus, referred to as unlabeled classes.

In general, AD is performed in a completely blind environment. Two main issues must be addressed: 1) how to find anomalies without using any prior knowledge and 2) how to discriminate one anomaly from another once anomalies are detected. As for the first issue, many efforts have been reported in [8], [20], and [37] such as RXD originally developed in [2] along with its variants developed in [8]. However, all these anomaly detectors suffer from a common issue that requires an appropriate threshold value to segment anomalies out from the background (BKG) because AD-detection maps are generally real valued. To address the second issue, a recent work on anomaly discrimination and categorization was developed in [37] and [38]. But it stopped short on how to classify anomalies using spatial information among anomalies. The *a posteriori* AD presented in this paper is developed to fill in this missing piece.

Before moving on, it is important to clarify several terminologies used in this paper. AD detects targets which are generally spectrally distinct from their surroundings. Anomaly discrimination discerns detected anomalies one from another using some discrimination measure such as spectral angle mapper (SAM) or spectral information divergence (SID) [1]. A general terminology widely used in remote sensing community is anomaly clustering, which groups detected anomalies according to a certain clustering rule such as  $k$ -nearest neighboring rule, Euclidean distance, and SAM or SID into different clusters. The concept of anomaly categorization was originally developed in [37] and [38], which groups detected anomalies into different categories. Here, we would like to point out that there is a distinction between “category” and “cluster.” A “cluster” is a set of data sample vectors being grouped by comparing one data sample vector to another data sample vector using a specific clustering rule. A category is a set of data sample vectors being specified by a particular means such as an algorithm, but not grouped by comparisons as clustering does. In addition, it should be also noted that a category is different from a class. A class is a set of data sample vectors being grouped by a rule which takes the advantage of spatial information among data sample vectors. When there is a class label assigned to it, it is called a labeled class. Otherwise, it is called an unlabeled class. UAC classifies detected anomalies using their surrounding spatial information without prior knowledge where each classified anomaly class is unlabeled. Fig. 1 depicts their relationships. However, we would like to point out that the taxonomy provided in Fig. 1 is simply based on the authors’ personal preference and clarification, and the definitions in Fig. 1 are by no means standard terminologies.

To illustrate Fig. 1, the following example should suffice to illustrate differences among the definitions given in Fig. 1. Suppose that in a battle field, there have various vehicles of different types, such as tracked vehicles and wheeled vehicles. AD is to detect vehicles regardless of the types of vehicles. Anomaly discrimination differentiates one type of vehicles from another. Anomaly clustering groups vehicles according to tracked or wheeled vehicles. Anomaly categorization further separates tracked vehicles into different categories of tracked vehicles into trucks, tanks, etc., and

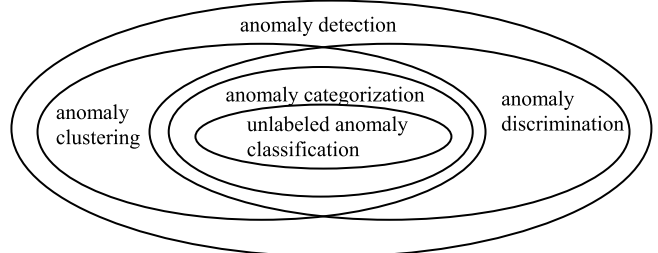


Fig. 1. Taxonomy of anomaly functionality.

different categories of wheeled vehicles into ten-wheel trucks, four-wheel cars, etc. UAC divides tanks into Russian-made tanks and U.S.-made tanks into different classes without specifically labeling either Russian-made or U.S.-made tanks due to unavailability of prior knowledge. It can also divide four-wheel cars into humvees and jeeps into different classes without class label assignment. Because of no prior knowledge being available, the classes are not labeled, referred to as unlabeled classes.

Using spatial information is crucial to classification. This is generally accomplished by using local windows which processes the original data samples falling in the windows to capture the spatial correlation. This type of AD is referred to as *a priori* AD. The proposed *a posteriori* AD looks into spatial information after processing data to produce anomalies i.e., the spatial information captured from neighboring data sample vectors surrounding detected anomalies. It is quite different from *a priori* AD using local windows simultaneously at the same time where the local spatial information is captured while AD is taking place. A major advantage of *a posteriori* AD over *a priori* AD is its use of spatial information obtained directly from AD maps to capture spatial information of detected anomalies rather than spatial information provided by original data samples *a priori*, but not necessarily detected anomalies.

The key idea of *a posteriori* AD is to introduce an iterative version of AD, called iterative anomaly detection (IAD), which is designed to capture *a posteriori* spatial correlation among detected anomalies right after AD. In doing so, IAD applies a spatial Gaussian filter to an AD map. The resulting Gaussian-filtered AD map contains crucial spatial information among detected anomalies and can be considered as a new band image added to the currently being processed hyperspectral image to create a new image cube to be used for reprocessing AD. Such a process forms a feedback loop that can be implemented iteratively to update *a posteriori* anomaly spatial information. That is, the more the feedbacks, the more is the *a posteriori* spatial information about detected anomalies. In other words, IAD uses a Gaussian filter to capture spatial correlation among detected anomalies in an AD map. Then, the Gaussian-filtered AD map is further fed back as a new hyperspectral band image to expand the current hyperspectral image cube by one spectral dimension for the next round process of AD. This additional band image provides crucial spatial correlation of detected anomalies that are missed in the original hyperspectral image cube. To further differentiate detected anomalies, ATGP is implemented in conjunction with AD at each iteration to identify spectrally distinct anomalies among detected anomalies. In order to terminate the iterative process carried out by

IAD, an automatic stopping rule is also introduced. At this terminal stage, the final set of distinct anomalies generated by IAD is used to specify particular anomaly classes without a label. These distinct anomalies are then used as desired target signatures for a follow-up subpixel target detection technique, constrained energy minimization (CEM) in [40]–[42] to produce real-valued abundance fractions of spectrally distinct anomalies. Finally, unlabeled anomaly classes are obtained by Otsu's method [43].

Several new ideas proposed in this paper have never been investigated in the past, even not in [37] and [39]. First and foremost is the introduction of *a posteriori* AD which captures *a posteriori* spatial information surrounding detected anomalies not from original data samples using local windows. Second is developing IAD to be implemented as an iterative process to update *a posteriori* spatial information about detected anomalies. It is believed that IAD is the first work ever reported in the literature. Third, it takes advantage of an unsupervised target detection algorithm such as ATGP [10] to identify spectrally distinct anomalies, each of which specifies without labeling a particular anomaly class. Fourth, it uses the identified distinct anomalies as desired target signatures to implement CEM to generate abundance fractional maps of unlabeled anomalies. Last but not least, the last piece of UAC is to implement Otsu's method to threshold the real-valued CEM-detected anomaly abundance fractional maps to produce final unlabeled anomaly classes.

## II. ANOMALY DETECTION

This section briefly reviews two major anomaly detectors commonly used in the literature. One is RXD. Since it takes advantage of the inverse of the global data sample covariance matrix  $\mathbf{K}$  to perform BKG suppression, it is referred to as K-AD, denoted by  $\delta^{\text{K-AD}}(\mathbf{r})$  and specified by

$$\delta^{\text{K-AD}}(\mathbf{r}) = (\mathbf{r} - \boldsymbol{\mu})^T \mathbf{K}^{-1} (\mathbf{r} - \boldsymbol{\mu}) \quad (1)$$

where  $\mathbf{r}$  is a vector of a data sample,  $\boldsymbol{\mu}$  is the mean vector of data samples, and  $\mathbf{K}$  is the global sample covariance matrix. Equation (1) is actually the well-known Mahalanobis distance.

Another type of anomaly detector is developed in [1] and [8]. It is different from K-AD in the sense that the global sample data covariance matrix  $\mathbf{K}$  in (1) is replaced by the global sample data correlation matrix  $\mathbf{R}$ . It is defined by

$$\delta^{\text{R-AD}}(\mathbf{r}) = \mathbf{r}^T \mathbf{R}^{-1} \mathbf{r} \quad (2)$$

where the superscript of R-AD is used to indicate that AD is performed by  $\mathbf{R}^{-1}$  to suppress BKG to differentiate K-AD used in (1).

According to (1) and (2), K/R-AD produces real-valued AD map. It does not provide any means of how to discriminate anomalies one way or another. As a matter of fact, this issue poses a great challenge because of several major reasons. First of all, we need to determine what anomalies are because an AD map is generally real valued and requires an appropriate threshold to segment anomalies out from the BKG. Second, once anomalies are found, how to tell them apart. Third, with no availability of prior knowledge, there is no way to know how many types of anomalies needed to be

discriminated. Fourth, since anomalies distinguish themselves from their surroundings, their presence is closely related to spatial correlation with their neighboring pixels. Apparently, addressing this issue is not trivial. This is because K-AD and R-AD are performed on a pixel basis without taking into account sample correlation among anomalies. In Section III, we will develop an approach to UAC to resolve all the above issues where anomalies can be classified into unlabeled classes without prior knowledge.

## III. FINDING SPECTRALLY DISTINCT ANOMALY CLASSES

As noted above, the detection maps produced by anomaly detectors specified by (1) and (2) are real valued. In order to detect anomalies, an appropriate threshold is needed to determine whether the data sample vector is an anomalous pixel or a BKG pixel. Unfortunately, finding such a threshold is very challenging, and up to now there are no guideline or automatic methods provided for this purpose. This section deviates from the idea of finding a threshold. Instead, it looks into an approach that can automatically determine and generate a set of spectrally distinct anomalies.

Let  $L$  be the total number of spectral bands used to acquire a hyperspectral image. According to the concept of virtual dimensionality (VD) introduced in [1] and [44], a spectrally distinct signature can be accommodated by a particular spectral band. With this interpretation, there are only  $L$  distinct types of anomalies that can be differentiated by an  $L$ -band hyperspectral image. In this case, the only data sample vectors of interest for anomaly classification would be those with the first  $L$  largest magnitudes produced by anomaly detectors.

### A. ATGP for Finding Spectrally Distinct Detected Anomalies for R-AD

Theoretically, the information provided by two distinct data sample vectors should be mutually orthogonal. This implies that two data sample vectors should be orthogonal. Using this fact, one best criterion to measure two different data sample vectors is orthogonal projection (OP). An algorithm designed based on OP is ATGP (Algorithm 1) which can be used for this purpose. It is an OP-based unsupervised target detection which repeatedly finds maximal residuals from a successive OP subspace.

---

#### Algorithm 1 ATGP

---

1. Initialization of ATGP: find the first target vector with largest energy:

$$\mathbf{t}_1^{\text{ATGP}} = \arg \left\{ \max_{\mathbf{r}} \mathbf{r}^T \mathbf{r} \right\} \quad (3)$$

2. For each  $2 \leq l \leq L$ , find the target pixels as follows:

$$\mathbf{t}_l^{\text{ATGP}} = \arg \left\{ \max_{\mathbf{r}} \mathbf{r}^T P_{\mathbf{U}_{l-1}}^{\perp} \mathbf{r} \right\} \quad (4)$$

where  $\mathbf{U}_{l-1} = [\mathbf{t}_1^{\text{ATGP}} \mathbf{t}_2^{\text{ATGP}} \dots \mathbf{t}_{l-1}^{\text{ATGP}}]$  and

$$P_{\mathbf{U}_{l-1}}^{\perp} = \mathbf{I} - \mathbf{U}_{l-1} \left( \mathbf{U}_{l-1}^T \mathbf{U}_{l-1} \right)^{-1} \mathbf{U}_{l-1}^T. \quad (5)$$


---

### B. Eigenvectors for Finding Spectrally Distinct Detected Anomalies for K-AD

Since K-AD algorithm removes the global sample mean, it is a second-order statistics anomaly detector. In this case, an unsupervised target distinction algorithm to determine if K-AD-found targets are anomalies should not rely on the sample mean. One way to solve this problem is to use eigenvectors (EVs) as a means of finding unsupervised target vectors in a similar manner that ATGP is selected for R-AD because EVs are also mutually orthogonal.

Assume that  $\{\mathbf{v}_l\}_{l=1}^L$  is a set of EVs corresponding to a set of  $L$  eigenvalues  $\{\lambda_l\}_{l=1}^L$  calculated from the sample autocovariance matrix  $\mathbf{K}$ . Since distinct eigenvalues will produce orthogonal EVs, these EVs can be used to identify spectrally distinct data sample vectors. We then use EVs to find data sample vectors yielding the maximal projections along each of EVs  $\{\mathbf{v}_l\}_{l=1}^L$  as follows:

$$\mathbf{t}_l^{\text{EV}} = \arg \left\{ \max_{\mathbf{r}} |(\mathbf{r} - \boldsymbol{\mu})^T \mathbf{v}_l| \right\} \quad \text{for each } 1 \leq l \leq L \quad (6)$$

which plays a similar role as  $\mathbf{t}_l^{\text{ATGP}}$  in (4) does for R-AD.

### IV. ITERATIVE ANOMALY DETECTION

As noted, anomalies are generally spatially correlated with their surrounding data sample vectors. It would be beneficial to include spatial information into finding anomalies. Unfortunately, K-AD in (1) and R-AD in (2) do not take into account local spatial correlation and neither does anomaly categorization in [37] and [38]. To capture such local spatial properties, this section develops an iterative version of AD, to be called IAD, which includes Gaussian filters to smooth AD-generated detection maps and further feed the Gaussian-filtered detection maps back to form a new hyperspectral image cube for AD to be reimplemented over again in an iterative manner. Algorithm 2 details its ideas where AD can be either R-AD or K-AD.

---

### Algorithm 2 Iterative Anomaly Detection (IAD)

---

- Initial condition:  
Let  $\Omega^{(0)} = \{\mathbf{B}_l\}_{l=1}^L$  be the original hyperspectral image cube. Let  $\{\mathbf{r}_i^{(0)} = (r_{i1}, \dots, r_{iL})^T\}_{i=1}^N$  be data sample vectors in  $\Omega^{(0)}$ . Let  $\delta_0^{\text{AD}}$  be an AD (K-AD/R-AD) operating on  $\Omega^{(0)}$  and  $k = 0$ .
  - Let  $k = k + 1$ . At the  $k^{\text{th}}$  iteration, use a Gaussian filter to blur  $|\mathbf{B}|_{\text{AD}}^{(k)}$ , where  $|\mathbf{B}|_{\text{AD}}^{(k)}$  is the absolute value of the detection map produced by  $\delta_{k-1}^{\text{AD}}$ ,  $\mathbf{B}_{\text{AD}}^{(k)}$ . The resulting image is denoted by Gaussian-filter  $|\mathbf{B}|_{\text{GFAD}}^{(k)}$ .
  - Form  $\Omega^{(k)} = \Omega^{(k-1)} \cup \{|\mathbf{B}|_{\text{GFAD}}^{(k)}\}$ . Find representatives for anomaly classes  $T^{(k)}$  using the algorithms proposed in Section III.
  - Check if  $T^{(k)}$  satisfies a given stopping rule. If no, back to step 2. Otherwise, go to step 5.
  - $T^{(k)}$  is the data set with desired target signatures and IAD is terminated.
- 

### V. AUTOMATIC STOPPING RULE FOR IAD

In order to terminate IAD, it will require a stopping rule. This section derives an idea which takes advantage of ATGP for R-AD (or EV for K-AD) to identify spectrally distinct anomalies from Gaussian-filter AD-detection maps generated iteratively by IAD until the number of such identified spectrally distinct anomalies converges. The details of step-by-step implementations of the stopping rule are described in Algorithm 3.

---

### Algorithm 3 Stopping Rule for IAD

---

- Use  $\delta_k^{\text{AD}}$  in IAD to find  $L$  maximum gray-scales detection values in descending order in terms of vector length from the corresponded hyperspectral image  $\Omega^{(k)}$ , i.e.,  $||\mathbf{t}_1^{\text{AD}(k)}|| \geq ||\mathbf{t}_2^{\text{AD}(k)}|| \geq \dots \geq ||\mathbf{t}_L^{\text{AD}(k)}||$
  - Apply ATGP for R-AD to  $\Omega^{(k)}$  (or find EV for K-AD) to generate  $L$  target pixels, denoted by  $\{\mathbf{t}_l^{\text{ATGP/EV}(k)}\}_{l=1}^L$ .
  - Find  $T^{(k)} = \{\mathbf{t}_l^{\text{AD}(k)}\}_{l=1}^L \cap \{\mathbf{t}_l^{\text{ATGP/EV}(k)}\}_{l=1}^L = \{\mathbf{t}_j^{\text{A}(k)}\}_{j=1}^{\tilde{L}}$  where  $\tilde{L} \leq L$  is the number of different classes of anomalies.
  - If  $T^{(k+1)} = T^{(k)}$ , then the algorithm is terminated. Otherwise, go to step 1.
- 

### VI. UNLABELED ANOMALY CLASSIFICATION BY IAD

The idea of UAC is to process IAD which feeds back spatial information of anomalies to account for local properties of anomalies. The stopping rule is to produce a final set of spectrally distinct anomalies, each of which represents a particular target class. Implementing IAD in Section IV in conjunction with the stopping rule proposed in Section V gives rise to UAC as described in Algorithm 4.

---

### Algorithm 4 Unlabeled Anomaly Classification (UAC)

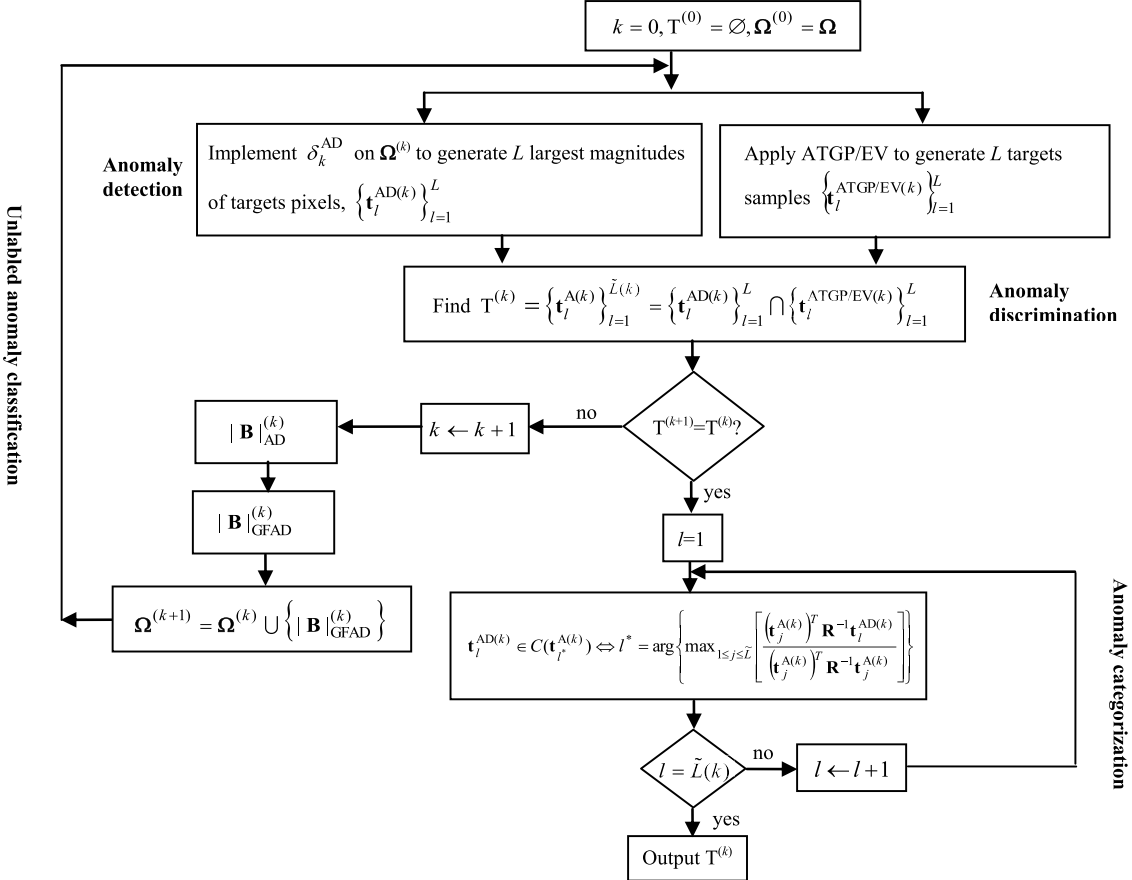
---

- Implement IAD in Section IV.
  - Use the stopping rule in Section V to produce a final target set  $T^{(k)}$ , denoted by  $T^{(k)} = \{\mathbf{t}_j^{\text{A}(k)}\}_{j=1}^{\tilde{L}}$
  - For each  $\mathbf{t}_j^{\text{A}(k)}$  in  $T^{(k)}$ , constrained energy minimization (CEM) developed in [40-42] uses it as a desired target signature to produce a detection map to classify  $\mathbf{t}_j^{\text{A}(k)}$ , denoted by  $\mathbf{B}_{\text{CEM}}^{(j)}$ .
  - For each  $\mathbf{B}_{\text{CEM}}^{(j)}$  for  $j = 1$  to  $\tilde{L}$ , use Otsu's method for thresholding and get the final target classification maps.
- 

A flowchart of implementing *a posteriori* AD with details is diagramed in Fig. 2, where the functionalities of AD, anomaly discrimination, anomaly categorization, and UAC are clearly indicated. Fig. 3 also provides a graphical representation to illustrate the implementation of UAC.

### VII. SYNTHETIC IMAGE EXPERIMENTS

This section conducts synthetic image experiments using an airborne visible infrared imaging spectrometer (AVIRIS)

Fig. 2. Flowchart of *a posteriori* AD.

Cuprite image data shown in Fig. 4(a), which is available on the NASA website <http://aviris.jpl.nasa.gov/> with found in [37], [38], and [45]. There are five minerals: Alunite (A), Buddingtonite (B), Calcite (C), Kaolinite (K), and Muscovite (M) labeled A, B, C, K, and M, respectively, specified by five pixels shown in Fig. 3(a) with their spectra shown in Fig. 4(b) to be used to simulate 25 panels shown in Fig. 4(c) according to the legends described. The sample mean of an area marked by “BKG” at the top right corner of Fig. 4(a), denoted by  $\mathbf{b}$  and plotted in Fig. 3(b), is used to simulate BKG for image scene in Fig. 4(c). This  $\mathbf{b}$ -simulated image BKG is further corrupted by an additive noise to achieve a certain signal-to-noise ratio (SNR) which is defined as 50% signature (i.e., reflectance/radiance) divided by the standard deviation of the noise in [46]. Once target and BKG pixels are simulated, two types of target insertion, referred to as target implantation (TI) and target embeddedness (TE), are designed to simulate experiments for various applications.

#### A. TI Experiments

TI is simulated by inserting clean target panels into a noisy image BKG by replacing their corresponding BKG pixels where the SNR is set to 20:1. That is, TI implants clean target panel pixels into noise-corrupted image BKG with SNR = 20:1. UAC is first initialized by implementing R-AD and ATGP on TI where Fig. 5(a) and (b) shows the anomalous pixels with the first 189 largest magnitudes found by  $\delta_0^{R-AD}$ ,  $\{t_j^{R-AD(0)}\}_{j=1}^{189}$ , and the 189 target pixels found by ATGP,

TABLE I  
NUMBER OF TARGETS GENERATED AT EACH ITERATION BY ATGP VIA UAC FOR TI

# of iterations	0	1	2	3	4	5
# of anomalous targets	37	28	24	19	17	17

$\{t_j^{ATGP(0)}\}_{j=1}^{189}$ , respectively, and intersection of target pixels found in Fig. 5(a) and (b)  $T^{(0)} = \{t_j^{A(0)}\}_{j=1}^{37} = \{t_j^{R-AD(0)}\}_{j=1}^{189} \cap \{t_j^{ATGP(0)}\}_{j=1}^{189}$  is shown in Fig. 5(c) with  $\tilde{L} = 37$ .

Now let  $\mathbf{B}_{R-AD}^{(1)}$  be the R-AD detection map produced by  $\delta_0^{R-AD}$ , where superscript “(1)” in  $\mathbf{B}_{R-AD}^{(1)}$  indicates the detection map produced by applying R-AD to original hyperspectral data set  $\delta_0^{R-AD}$  to TI as an initial AD map. Then, a Gaussian filter with a window size of  $11 \times 11$  and  $\sigma = 0.1$  was applied to  $|\mathbf{B}|_{R-AD}^{(1)}$  which is the absolute values of  $\mathbf{B}_{R-AD}^{(1)}$  to produce a new band image  $|\mathbf{B}|_{GFR-AD}^{(1)}$  which includes Gaussian-filtered spatial information. This  $|\mathbf{B}|_{GFR-AD}^{(1)}$  is then included into the original hyperspectral image cube  $\Omega^{(0)}$  as a new band image to create a new hyperspectral image cube  $\Omega^{(1)}$  formed by  $\Omega^{(1)} = \Omega^{(0)} \cup \{|\mathbf{B}|_{GFR-AD}^{(1)}\}$  to be used as a hyperspectral image cube for the next iteration carried out by  $\delta_1^{R-AD}$ . The same process was repeated over again until it satisfied the stopping rule described in Section V. Table I tabulates the number of iterations and the number of anomalous targets identified by ATGP via *a posteriori* AD for TI which was terminated at the fifth iteration, and a total of 17 target pixels are determined

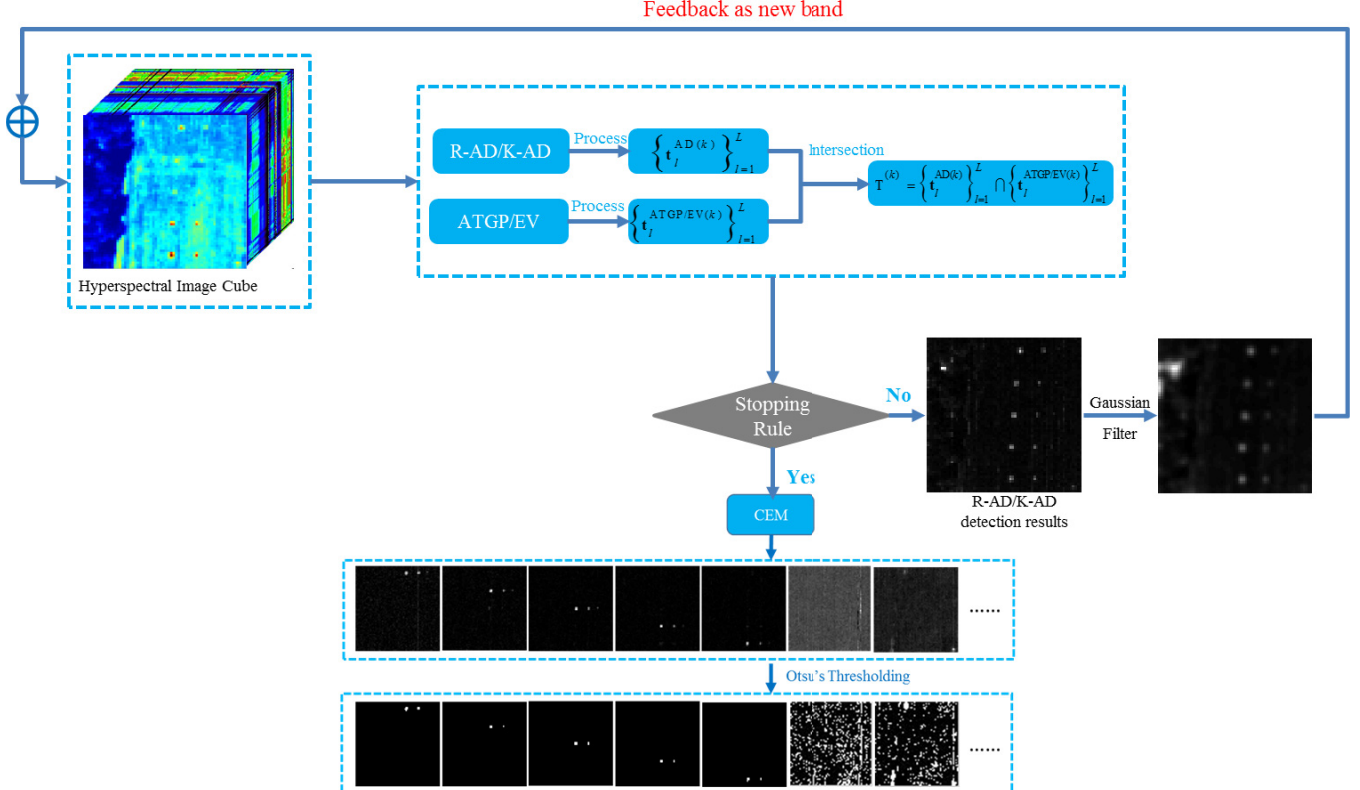


Fig. 3. Graphical representation for illustration of target classification by UAC.

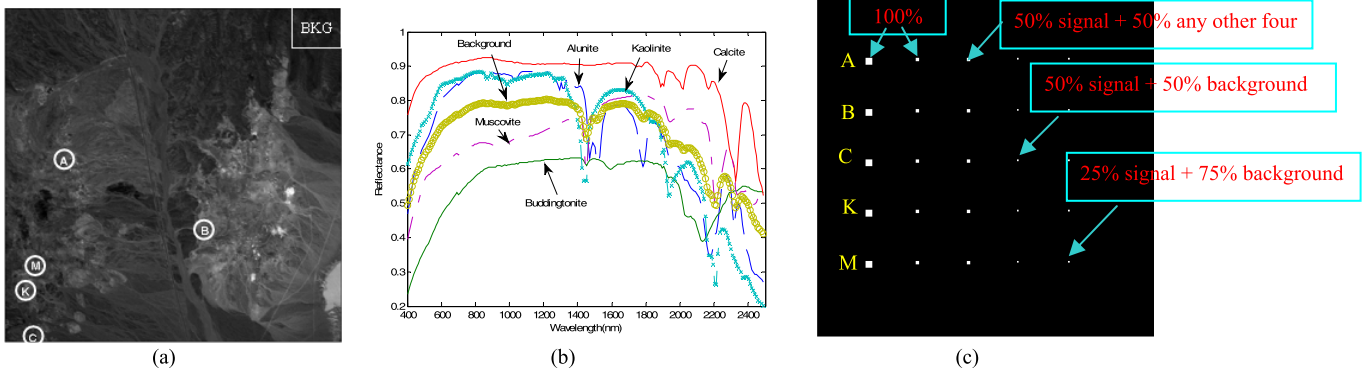


Fig. 4. (a) Cuprite image scene of AVIRIS. (b) Five mineral reflectance spectra signatures and BKG signature obtained using the average of top right region in (a). (c) The distribution of 25 panels simulated by A, B, C, K, and M.

and shown in Fig. 6 where the iteration #0 indicates the initial number of anomalous targets identified by  $\delta_0^{R-AD}$  and ATGP in Fig. 5(a).

As shown in Fig. 6, the first five UAC-found anomalous targets were all at the top left corners of the  $4 \times 4$  panels in the first column, each of which corresponds one of the five minerals, while the remaining 12 pixels seemed to be BKG as shown in Fig. 8.

From the classification maps in Fig. 8, it is clearly shown that the first five detection maps corresponded to five minerals in different rows and the remaining 12 detection maps were

actually BKG classes. It should be noted that the pure panels in the first and second columns and mixed pixels in the third column were classified as anomalous pixels in the first five detection maps. Interestingly, all the subpixel targets located in the fourth column were classified as anomalies separately, but none of subpixel targets in the fifth column were detected as anomalies since the target signatures in the fifth column are too weak to be detected.

To further conduct a detailed analysis on how UAC performs anomaly unlabeled classification on the 130 inserted panel pixels, Fig. 9 fuses the results of the first five classification maps in Fig. 8 into one classification map using five different colors, each of which corresponds to one particular unlabeled anomaly class. Since there is no prior knowledge provided regarding class label information, the anomaly classes were

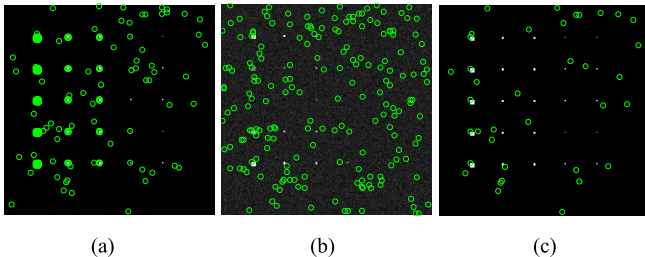


Fig. 5. Initialization of a posteriori AD by R-AD coupled with ATGP for TI. (a)  $\{t_j^{R\text{-AD}(0)}\}_{j=1}^{189}$ . (b)  $\{t_j^{ATGP(0)}\}_{j=1}^{189}$ . (c)  $\{t_j^{A(0)}\}_{j=1}^{37}$ .

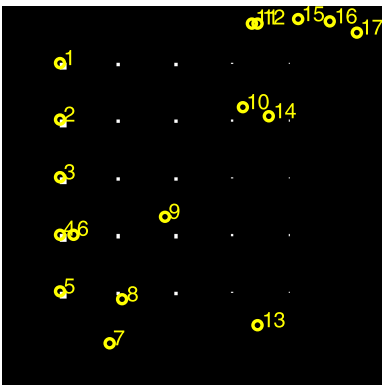


Fig. 6. Seventeen targets found by UAC using ATGP.

identified and assigned to the orders that the target pixels were generated by ATGP to find their corresponding anomaly classes. According to Fig. 9, all the 100 pure panel pixels in the first and second columns and five panel subpixels in the fourth column were detected as anomalies and assigned to their correct respective anomaly classes. Most interestingly, due to the fact that the 20 panel pixels in the third column were mixed by different mineral signatures according to the legends described in Fig. 4(c), as expected, most of these mixed panel pixels were identified and assigned to two classes as shown in Fig. 9 where a mixed panel pixel marked by a pair of  $x$ ,  $y$  indicated that this mixed pixel was detected as an anomaly but assigned to two anomaly classes specified by  $x$  and  $y$ . For example, four mixed panel pixels in row 1 and column 3 were simulated by 50% of the mineral signature A and identified as anomaly class 1. So, it is natural to note that all the four mixed pixels were identified as anomalies and assigned to class 1. But due to the other 50% of mixture with other mineral signatures, these four mixed pixels would also be assigned to a second anomaly class with the pixels at the top left corner assigned to classes 1 and 2, bottom left corner assigned to classes 1 and 4, top right corner assigned to a single class 1, and bottom right corner assigned to classes 1 and 5. In addition, the panel subpixels in the fifth column were not detected as anomalies due to their weak energies.

The results in Fig. 9 show that UAC was able to correctly classify 125 out of 130 simulated panel pixels but only missed five panel subpixels in the fifth column because their abundance fractions were simulated by only 25% of mineral signatures which were too weak to be detected as anomalies.

TABLE II

NUMBER OF TARGETS GENERATED AT EACH ITERATION BY ATGP VIA UAC FOR TE

# of iteration	0	1	2	3	4	5
# of anomalous targets	38	32	25	21	20	20

### B. TE Experiments

TE is simulated by embedding clean target panels into a noisy image BKG with superimposing target panel pixels over the BKG pixels where the SNR is set to 20:1. Similar experiments conducted for TI were also performed for TE. Fig. 10(a) and (b) shows the initial results of UAC produced by  $\delta_0^{R\text{-AD}}$  and ATGP, where the 189 anomalous pixels found by  $\delta_0^{R\text{-AD}}$  and 189 target pixels found by ATGP, respectively, and their intersection is shown in Fig. 10(c) with  $\tilde{L} = 38$ .

Assume that  $\mathbf{B}_{R\text{-AD}}^{(1)}$  is the detection map produced by  $\delta_0^{R\text{-AD}}$ , where “0” means R-AD operated on the original data set. Then, a Gaussian filter with a window size of  $11 \times 11$  and  $\sigma = 0.1$  was applied to the absolute values of  $\mathbf{B}_{R\text{-AD}}^{(1)}$  in Fig. 10(a),  $|\mathbf{B}|_{R\text{-AD}}^{(1)}$  to produce a new Gaussian-filtered band image  $|\mathbf{B}|_{GFR\text{-AD}}^{(1)}$  which is further included into the original hyperspectral image cube  $\Omega^{(0)}$  to create a new hyperspectral image cube  $\Omega^{(1)} = \Omega^{(0)} \cup \{|\mathbf{B}|_{GFR\text{-AD}}^{(1)}\}$ . The same process was then repeated over again until it satisfied the stopping rule described in Section V.

Table II tabulates the number of iterations and the number of anomalous targets identified by ATGP via UAC for TE which was terminated at the fifth iteration, and a total of 20 target pixels are determined and shown in Fig. 11.

As shown in Fig. 11, the first UAC-found target pixel seemed to be BKG pixel and the second–sixth IAD-found target pixels were all the top left corners of the  $4 \times 4$  panels in the first column, each of which corresponds one of the five minerals, while the remaining 14 pixels were all BKG pixels. The 20 target pixels in Fig. 11 were then used as desired signatures for CEM to produce 20 real-valued CEM-detection maps in Fig. 12. In order to perform target classification, Otsu’s method was further used to extract targets from BKG as shown in Fig. 12.

From the 20 target classification maps in Fig. 13, it is obvious that only the second–sixth classification maps were meaningful, each of which corresponded to one of the five minerals in five different rows, while the others were BKG pixels. Similar conclusion drawn by TI experiments can also be applied where the pure and mix panel pixels in the first–third columns of TE were classified correctly. Subpixels with strong target energy in the fourth column were also classified correctly, while weak subpixels in the fifth column were overwhelmed by BKG and could not be detected as target pixels.

Following a treatment similar to that used to discuss the TI experiments, a detailed analysis on how UAC performs anomaly unlabeled classification on the 130 inserted panel pixels was also conducted. Fig. 14 fuses the results from the second classification map up to sixth classification map

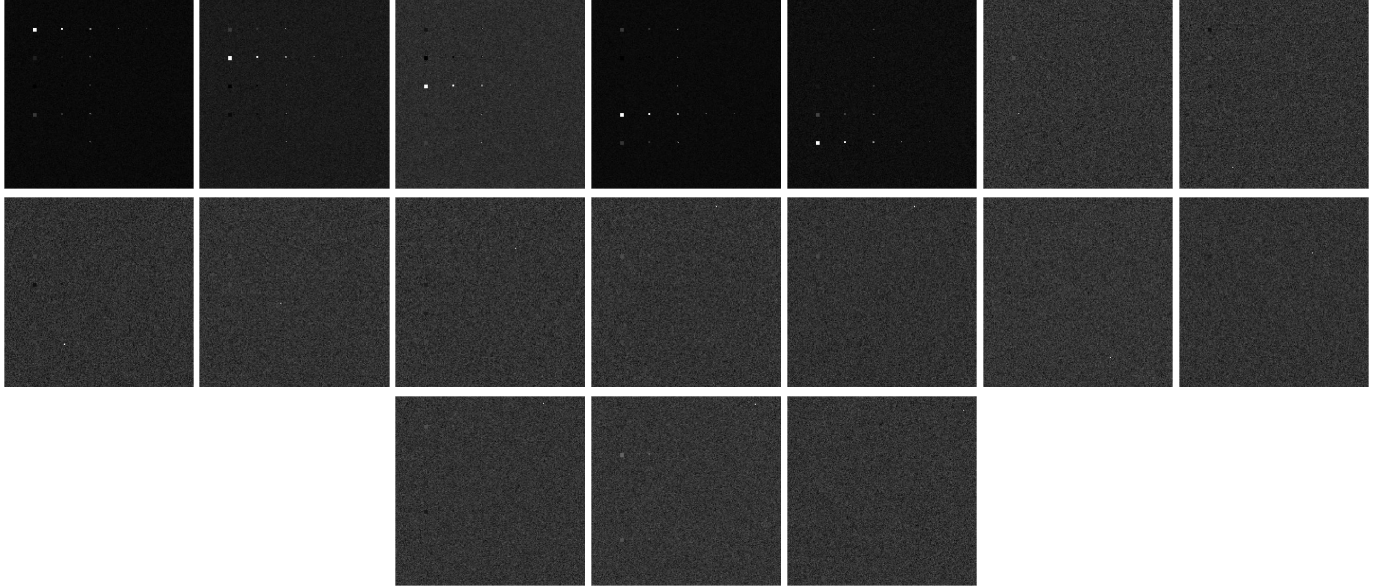


Fig. 7. Seventeen CEM-detection maps using the 17 signatures found in Fig. 6.

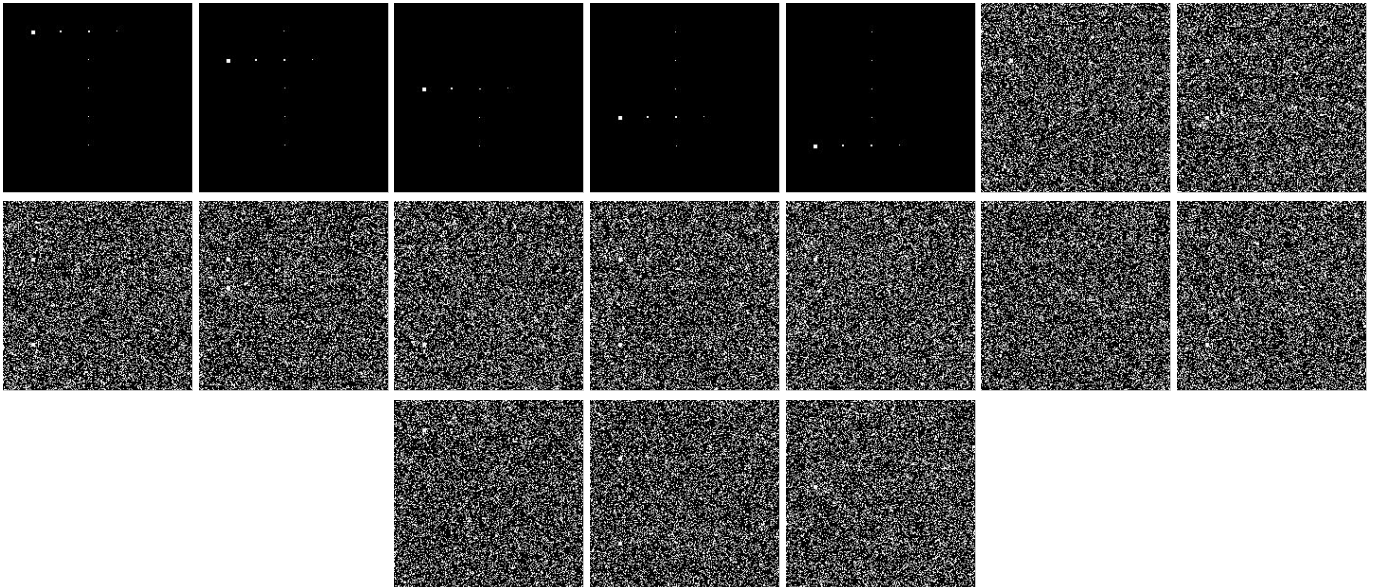


Fig. 8. Seventeen target-class classification maps by applying Otsu's method to 17 CEM-detection maps in Fig. 7.

in Fig. 13 into one classification map using five different colors, each of which corresponds to one particular unlabeled anomaly class. Once again, since there is no prior knowledge provided regarding class label information, the anomaly classes were identified and assigned to the orders that the target pixels were generated by ATGP to find their corresponding anomaly classes.

In analogy with the 20 mixed panel pixels in the TI scenario, the 20 panel pixels in the third column in the TE scenario were also mixed by different mineral signatures according to the legends described in Fig. 4(c). As a consequence, most of these mixed panel pixels were identified and assigned to two classes as shown in Fig. 14 where a mixed panel pixel marked by a pair of  $x, y$  indicated that this mixed pixel was detected

as an anomaly but assigned to two anomaly classes specified by  $x$  and  $y$ .

Comparing Fig. 14 with Fig. 9, both results were very similar. That is, all the 100 pure panel pixels in the first and second columns and five panel subpixels in the fourth column were detected as anomalies and assigned to their correct respective anomaly classes, and the panel subpixels in the fifth column were not detected as anomalies due to their weak energies. In other words, UAC was able to correctly classify 125 out of 130 simulated panel pixels and only missed five panel subpixels in the fifth column because their abundance fraction were simulated by only 25% mineral signatures which were too weak to be detected as anomalies.

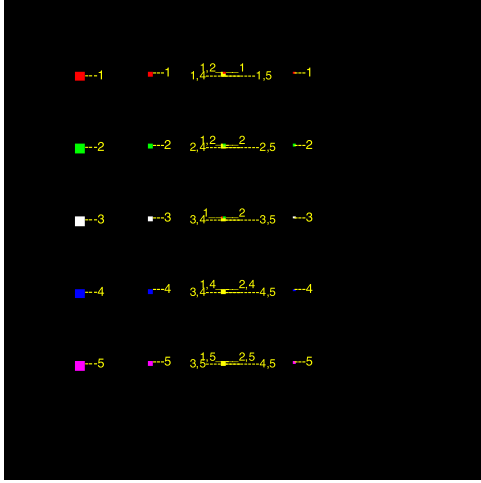


Fig. 9. Anomaly classes identified by UAC for TI.

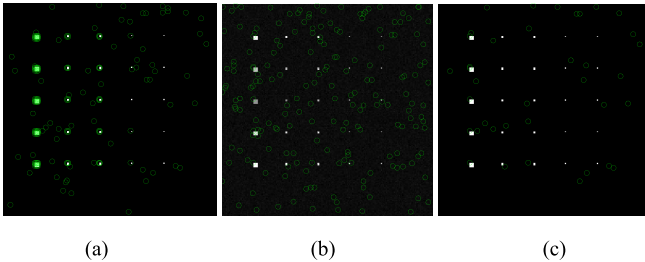
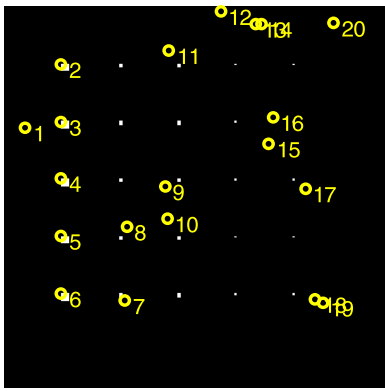
Fig. 10. Initialization of a posteriori AD by R-AD coupled with ATGP for TE. (a)  $\{t_j^{R\text{-AD}(0)}\}_{j=1}^{189}$ . (b)  $\{t_j^{ATGP(0)}\}_{j=1}^{189}$ . (c)  $\{t_j^{A(0)}\}_{j=1}^{38}$ .

Fig. 11. Twenty targets found by UAC using ATGP.

### VIII. REAL IMAGE EXPERIMENTS

In this section, we further conduct real hyperspectral image experiments to demonstrate the utility of the developed UAC in real applications. In particular, we consider two types of AD, R-AD coupled with ATGP in Section III-A and K-AD coupled with EVs in Section III-B to be implemented in UAC, respectively.

The image scene shown in Fig. 15(a) is an airborne hyperspectral digital imagery collection experiment (HYDICE) data collected in August 1995 from a flight altitude of 10 000 ft with the ground sampling distance approximately 1.56 m. This scene has been studied extensively by many reports such as [1]

TABLE III

NUMBER OF TARGETS GENERATED BY EACH ITERATION USING ATGP VIA UAC FOR HYDICE DATA

# of iterations	0	1	2	3	4	5	6	7
# of anomalous targets	64	41	35	29	26	20	19	19

and [17]. It has a total of 169 bands which were used for the experiments with low-signal/high-noise bands: bands 1–3 and bands 202–210, and water vapor absorption bands: bands 101–112 and bands 137–153 removed. There are 15 panels with three different sizes  $3 \times 3$  m,  $2 \times 2$  m, and  $1 \times 1$  m with its ground truth provided in Fig. 15(b), where the center and boundary pixels of objects are highlighted in red and yellow, respectively. In particular, R panel pixels are denoted by  $p_{ij}$  with rows indexed by  $i = 1, \dots, 5$  and columns indexed by  $j = 1, 2, 3$  except that the panels in the first column with the second–fifth rows which are two-pixel panels, denoted by  $p_{211}, p_{221}, p_{311}, p_{312}, p_{411}, p_{412}, p_{511}$ , and  $p_{521}$ . The 1.56-m-spatial resolution of the image scene suggests that most of the 15 panels are one pixel in size. As a result, there are a total of 19 R panel pixels. Fig. 15(b) shows the precise spatial locations of these 19 R panel pixels, where red pixels (R pixels) are the panel center pixels and the pixels in yellow (Y pixels) are the panel pixels mixed with the BKG.

#### A. UAC Using R-AD Coupled With ATGP

Fig. 16(a) and (b) shows the results of the first iteration of UAC carried out by  $\delta_0^{R\text{-AD}}$  and ATGP, where 169 anomalous pixels  $\{t_j^{R\text{-AD}(1)}\}_{j=1}^{169}$  found by  $\delta_0^{R\text{-AD}}$  in Fig. 16(a) and 169 target pixels  $\{t_j^{ATGP(1)}\}_{j=1}^{169}$  found by ATGP in Fig. 16(b), respectively, and their intersection  $T^{(0)} = \{t_j^{A(0)}\}_{j=1}^{64} = \{t_j^{R\text{-AD}(0)}\}_{j=1}^{169} \cap \{t_j^{ATGP(0)}\}_{j=1}^{169}$  is shown in Fig. 16(c) with 64 target pixels  $\tilde{L} = 64$ .

Let  $\mathbf{B}_{R\text{-AD}}^{(1)}$  be the detection map produced by  $\delta_0^{R\text{-AD}}$  at the first iteration and the original hyperspectral image cube be denoted by  $\Omega^{(0)}$ . A Gaussian filter with a window size of  $11 \times 11$  and  $\sigma = 0.1$  was applied to the absolute values of  $\mathbf{B}_{R\text{-AD}}^{(1)}, |\mathbf{B}|_{R\text{-AD}}^{(1)}$ , to produce a new Gaussian-filtered band image  $|\mathbf{B}|_{GFR\text{-AD}}^{(1)}$  which is further included into  $\Omega^{(1)}$  to create a new hyperspectral image cube  $\Omega^{(1)} = \Omega^{(0)} \cup \{|\mathbf{B}|_{GFR\text{-AD}}^{(1)}\}$  for the next iteration carried by  $\delta_1^{R\text{-AD}}$ . The same process was repeated over again until it satisfied the stopping rule described in Section V. Table III tabulates the number of iterations and the number of anomalous targets in the HYDICE data identified by ATGP at each iteration via UAC which was terminated at the seventh iteration.

A total of 19 target pixels are determined and shown in Fig. 17, among which 7 R panel pixels,  $p_{11}, p_{12}, p_{212}, p_{221}, p_{312}, p_{411}$ , and  $p_{521}$ , were found as 16th, 17th, 15th, 13th, 14th, 11th, and 12th target pixels, respectively.

The 19 target pixels found in Fig. 17 were further used as desired signatures for CEM to produce 19 real-valued CEM-detection maps shown in Fig. 18. In order to perform target classification, Otsu's method was then used to segment targets out from BKG as shown in Fig. 19.

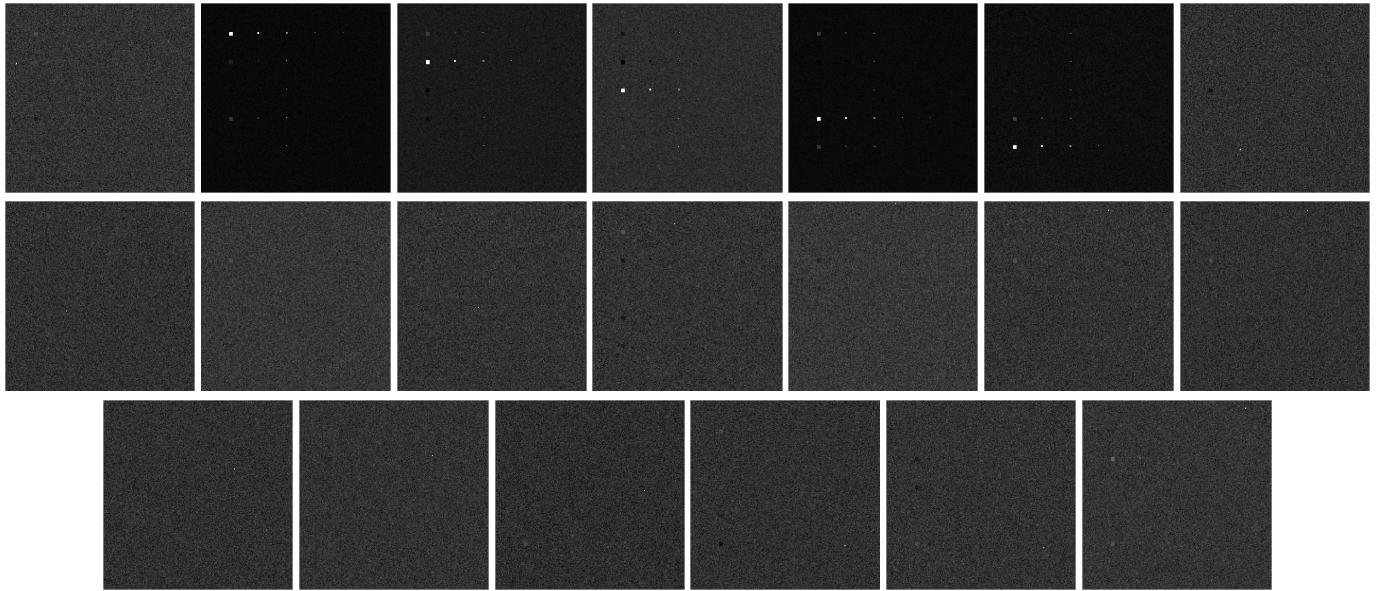


Fig. 12. Original gray-scale detection results of CEM algorithm using 20 signatures found in Fig. 11.

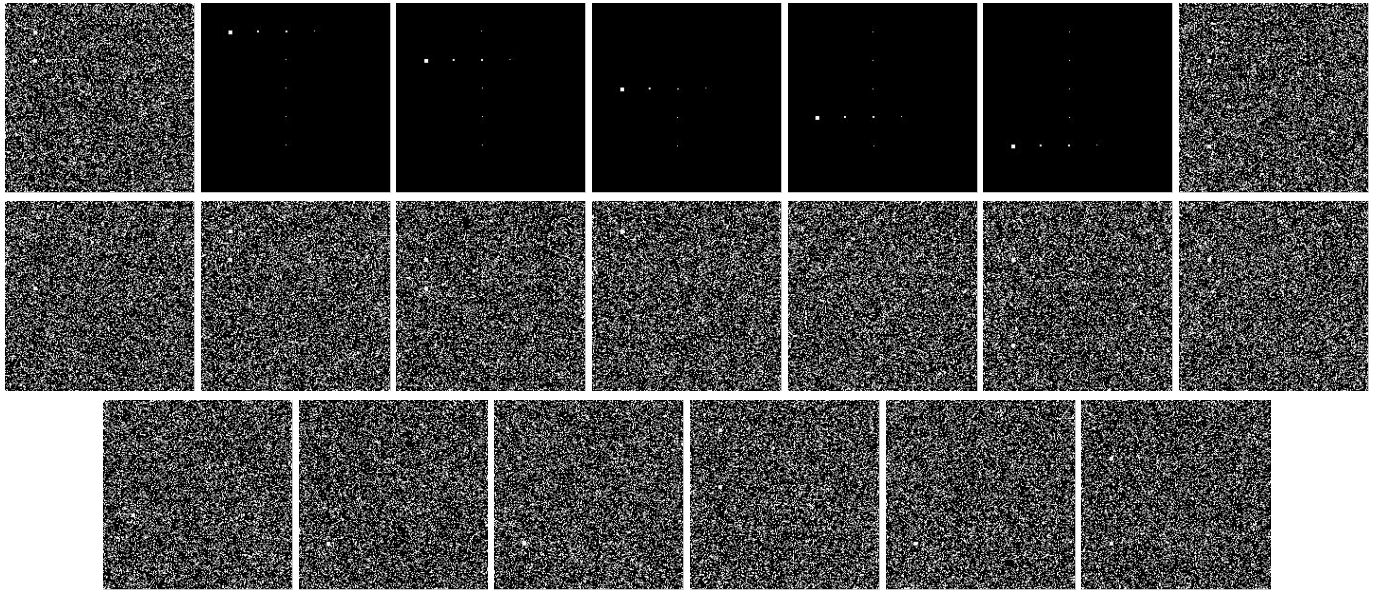


Fig. 13. Otsu's segmentation results for CEM results in Fig. 12.

According to Fig. 19, it is very obvious that the panel pixels in five rows were classified where panel pixels in the fourth, fifth, second, third, and first rows were classified in the 11th, 12th, 13th, 14th, and 16th in separate and individual classification maps in Fig. 19(k)–(q). It is interesting to note that the panel pixels in row 2 were classified in 13th and 15th classification maps in Fig. 19(m) and (o) because the 13th and 15th target pixels found by R-AD and ATGP were  $p_{211}$  and  $p_{212}$  in the same row 2. Similarly, the 16th and 17th target pixels were found to be  $p_{11}$  and  $p_{12}$  belonging to the same row 1. As a result, the 16th and 17th classification maps were used to classify panel pixels in row 1 in Fig. 19(p) and (q). In addition, the two interferences were also found in Fig. 19(d) and (e).

In order to further see how many panel pixels detected by UAC as anomalies, Fig. 20 fuses the results in Fig. 19(d) and (e) to find interferences identified as anomaly class 4, the results in Fig. 19(p) and (q) to find panel pixels in row 1 identified as anomaly class 16, the results in Fig. 19(m) and (o) to find panel pixels in row 2 identified as anomaly class 13, the result in Fig. 19(n) to find panel pixels in row 3 identified as anomaly class 14, the result in Fig. 19(k) to find panel pixels in row 4 identified as anomaly class 11, and the result in Fig. 19(l) to find panel pixels in row 5 identified as anomaly class 12. Since there is no provided prior knowledge about class labels, the anomaly class numbers were labeled by the orders that the target pixels were generated by ATGP to find anomaly classes. Interestingly, the two interferences were

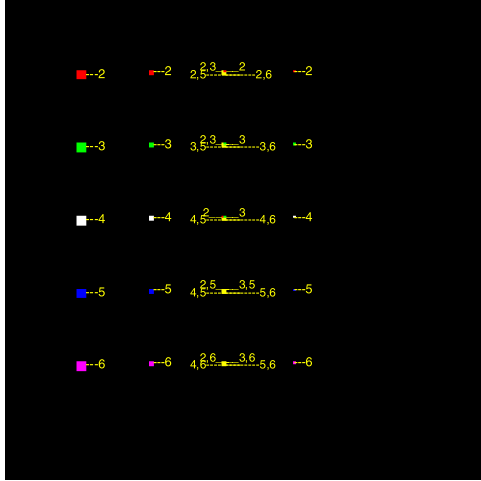


Fig. 14. Anomaly classes identified by UAC for TI.

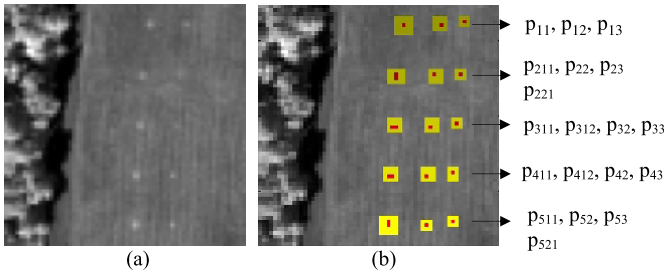
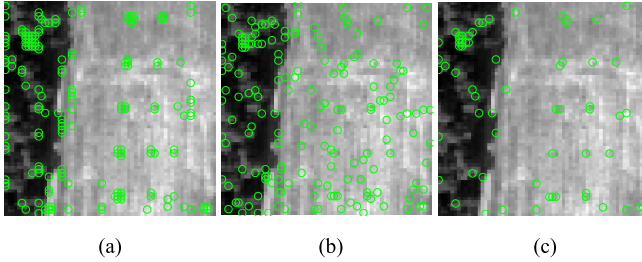


Fig. 15. (a) HYDICE panel scene which contains 15 panels. (b) Ground-truth map of spatial locations of the 15 panels.

Fig. 16. Results of the first iteration of UAC for HYDICE. (a)  $\{t_j^{R\text{-AD}(0)}\}_{j=1}^{169}$ . (b)  $\{t_j^{ATGP(0)}\}_{j=1}^{169}$ . (c)  $\{t_j^{A(0)}\}_{j=1}^{64}$ .

the first meaningful targets identified by UAC as an anomaly class labeled 4 shown in Fig. 19(d) and (e).

Specifically, Table IV tabulates the number of panel pixels in five rows in Fig. 15(b) detected as anomalies where a pair of  $(x, y)$  in Table IV indicates that there are  $x$  panel pixels in the first column and  $y$  panel pixels in the second column detected as anomalies. The last column in Table IV lists the anomaly classes to which panel pixels were assigned. Apparently, all panel subpixels in the third column of Fig. 15(b) were not detected as anomalies due to their weak appearance caused by small energies.

### B. UAC Using K-AD Coupled With Eigenvectors

Since K-AD removes the global sample mean and only uses second-order statistics, ATGP is not applicable to K-AD.

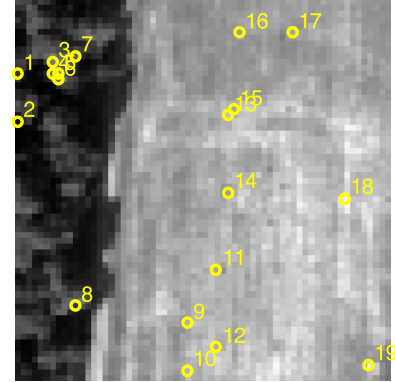


Fig. 17. Nineteen targets found by UAC using ATGP.

TABLE IV  
NUMBER OF PANEL PIXELS DETECTED AS ANOMALIES IN FIG. 20

	R panel pixels ( $x, y$ )	Yellow panel pixels ( $x, y$ )	Class #
panel pixels in row 1	(1,2)	(4,3)	16
panel pixels in row 2	(2,1)	(2,1)	13
panel pixels in row 3	(2,1)	(2,2)	14
panel pixels in row 4	(2,1)	(2,1)	11
panel pixels in row 5	(2,1)	(3,1)	12

As described in Section III-B, EVs were used to replace ATGP to do what ATGP does for R-AD.

Fig. 21(a) and (b) shows the results of the first iteration of UAC carried out by  $\delta_0^{K\text{-AD}}$  and EV, where 169 anomalous pixels  $\{t_j^{K\text{-AD}(1)}\}_{j=1}^{169}$  found by  $\delta_0^{K\text{-AD}}$  in Fig. 21(a) and 169 target pixels  $\{t_j^{EV(1)}\}_{j=1}^{169}$  found by EV in Fig. 21(b), and their intersection  $T^{(0)} = \{t_j^{A(0)}\}_{j=1}^{64} = \{t_j^{K\text{-AD}(0)}\}_{j=1}^{169} \cap \{t_j^{EV(0)}\}_{j=1}^{169}$  is shown in Fig. 21(c) with 64 target pixels.

Assume that  $\mathbf{B}_{K\text{-AD}}^{(1)}$  is the detection map produced by  $\delta_0^{K\text{-AD}}$  at the first iteration. Then, a Gaussian filter with a window size of  $11 \times 11$  and  $\sigma = 0.1$  was applied to the absolute values of  $\mathbf{B}_{K\text{-AD}}^{(1)}$  in Fig. 21(a),  $|\mathbf{B}_{K\text{-AD}}^{(1)}$ , to produce a new Gaussian-filtered band image  $|\mathbf{B}|_{GFK\text{-AD}}^{(1)}$  which is further included into the original hyperspectral image cube  $\Omega^{(0)}$  to create a new hyperspectral image cube  $\Omega^{(1)} = \Omega^{(0)} \cup \{|\mathbf{B}|_{GFK\text{-AD}}^{(1)}\}$  for the next iteration carried by  $\delta_1^{K\text{-AD}}$ . Then, the same process was repeated over again until it satisfied the stopping rule described in Section V. Unfortunately, IAD-K-AD was terminated at the second iteration which means that the target pixels found at the first iteration in Fig. 21(c) were the final target pixels. This implied that the spatial information captured by  $\mathbf{B}_{K\text{-AD}}^{(1)}$  did not help K-AD in target classification.

### IX. PARAMETER ANALYSIS FOR GAUSSIAN FILTERS

Finally, it is expected that the two parameters of a Gaussian filter, standard deviation  $\sigma$ , and window size used by UAC generally have impact on its performance. When these parameters vary, the results will also be different. These two issues were investigated in both synthetic data experiments and real HYDICE experiments where the Gaussian filter window size and  $\sigma$  were changed each time for comparison. Table V tabulates the number of anomalous targets found by UAC with

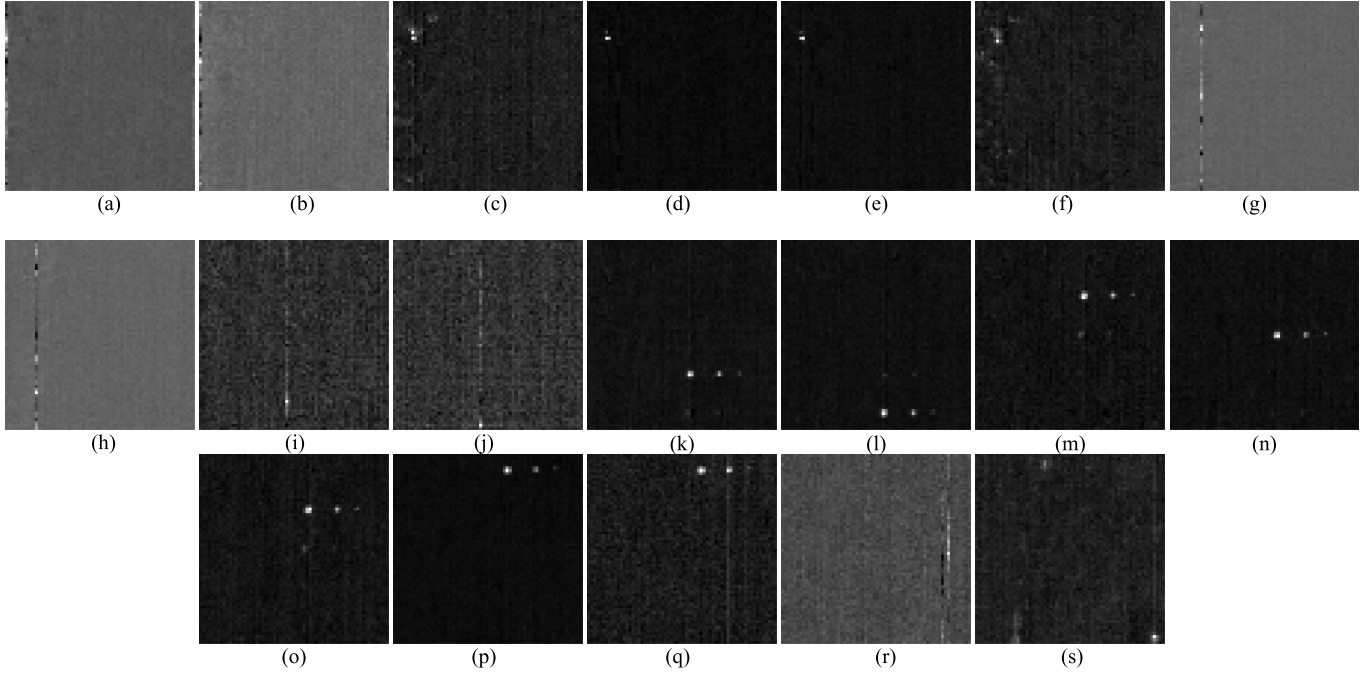


Fig. 18. Original gray-scale detection results of CEM algorithm using 19 signatures found in Fig. 17. (a) 1st target detection. (b) 2nd target detection. (c) 3rd target detection. (d) 4th target detection. (e) 5th target detection. (f) 6th target detection. (g) 7th target detection. (h) 8th target detection. (i) 9th target detection. (j) 10th target detection. (k) 11th target detection. (l) 12th target detection. (m) 13th target detection. (n) 14th target detection. (o) 15th target detection. (p) 16th target detection. (q) 17th target detection. (r) 18th target detection. (s) 19th target detection.

TABLE V  
NUMBER OF ITERATIONS AND NUMBER OF ANOMALOUS TARGETS FOUND BY UAC USING VARIOUS VALUES OF  $\sigma$

$\sigma$	TI						TE						HYDICE					
# of iterations	1	0.5	0.3	0.1	0.01	0.001	1	0.5	0.3	0.1	0.01	0.001	10	1	0.3	0.1	0.01	0.001
# of anomalous targets	-	4	5	5	5	5	-	5	5	5	5	5	7	13	7	7	7	7
	-	8	12	17	17	17	-	5	14	20	20	20	26	21	20	19	19	19

different values of  $\sigma$  where the number of found anomalous targets tended to be stable as the value of  $\sigma$  becomes small. On the other hand, the window size of Gaussian filter seemed to have little effect on the experimental results according to our extensive experiments.

Based on the results in Table IV, the proposed *a posteriori* AD is indeed robust to the used spatial Gaussian filter as long as the standard deviation  $\sigma$  is sufficiently small, for example,  $\sigma \leq 0.3$ .

As a final remark, a note on the noise issue in AD is worthwhile. According to our experience with the data sets used for experiments, the proposed UAC works effectively in the existence of noise since the SNR in hyperspectral imagery is generally very high in which case noise effect is not a problem. However, a more serious problem encountered in AD is not noise but rather unknown interference. This is something which needs to be addressed in hyperspectral target detection. Unfortunately, in practical applications, finding such unknown interferers and removing them is a very challenging issue.

## X. DISCUSSION

In this section, the following several issues arising from AD are addressed:

- 1) how to determine anomalies;
- 2) how to discriminate detected anomalies;

3) how to classify discriminated anomalies without labeling.

The first issue was previously investigated in [16]. A general approach is to use a threshold value to segment anomalies out from a detection map. However, this requires selecting an appropriate threshold. Since AD is generally carried out in a blind environment, finding such a threshold nearly impossible without prior knowledge. Even though a threshold is believed to be properly selected, the issue of whether or not the found anomalies are true anomalies still remains because the results cannot be verified and validated without ground truth which is generally not available in real-world applications. It is also noted that an effective anomaly detector does not imply that it can also determine anomalies. This is because the AD map generated by an anomaly detector is generally real valued and requires a threshold value to extract anomalies from the detection map.

Once anomalies are assumed to be found, the second issue is how to discriminate detected anomalies from one another. It seems that the recent work in [37] and [38] is the only approach to address the first and second issues all together. Unfortunately, this approach stopped short and did not address the third issue. The UAC proposed in this paper is developed to extend [37], [38] to resolve the issue of anomaly classification. Due to the fact that AD does not have any prior

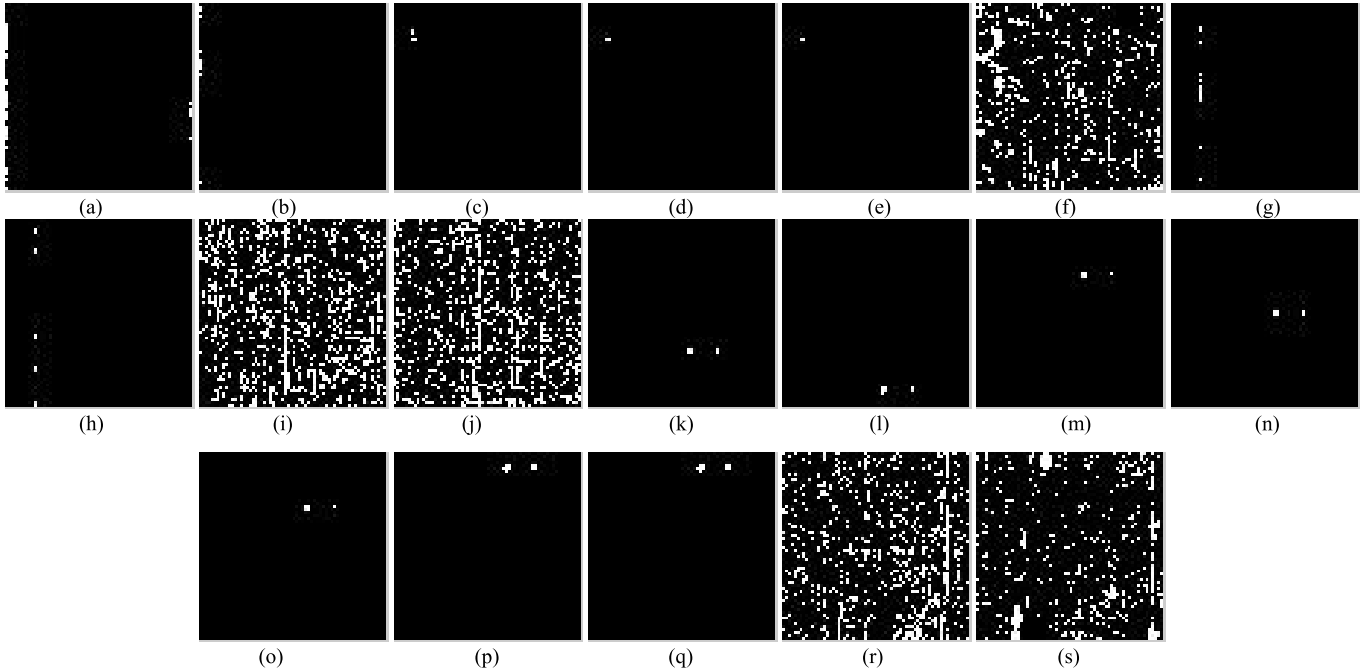


Fig. 19. Otsu's segmentation results for CEM results in Fig. 18. (a) 1st target classification. (b) 2nd target classification. (c) 3rd target classification. (d) 4th target classification(e) 5th target classification. (f) 6th target classification. (g) 7th target classification. (h) 8th target classification. (i) 9th target classification. (j) 10th target classification(k) 11th target classification. (l) 12th target classification. (m) 13th target classification. (n) 14th target classification. (o) 15th target classification. (p) 16th target classification(q) 17th target classification. (r) 18th target classification. (s) 19th target classification.

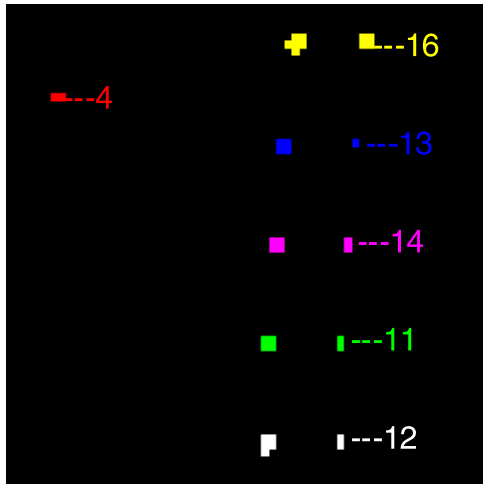


Fig. 20. Unlabeled anomaly classes identified by UAC.

knowledge with respect to targets of interest, anomaly classification cannot perform as traditional supervised membership-based classification. The UAC offers a bypass approach which can classify detected anomalies without actually labeling the classes it detected. As a result, the above three issues described in the beginning of this section can be solved by UAC using the following:

- 1) ATGP to determine anomalies;
- 2) CEM to discriminate detected anomalies;
- 3) IAD to classify discriminated anomalies.

The reason that a target is called an anomaly is because there is no provided prior knowledge of knowing whether or not it is an anomaly. This is one of the main issues in AD. Therefore, it is true that many targets detected in detection maps may not be anomalies by visual inspection as shown in Figs. 8, 13, and 19. But in reality, what we see as anomalies by

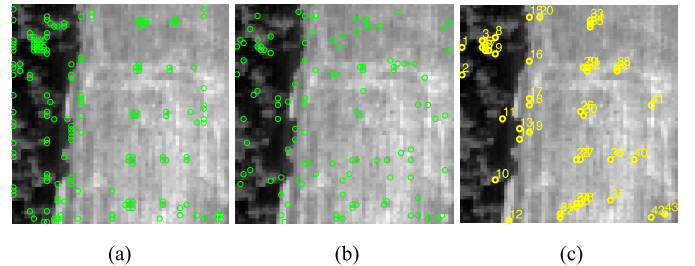


Fig. 21. AD, discrimination, and categorization by K-AD coupled with EV for HYDICE. (a)  $\{t_j^{K\text{-AD}(0)}\}_{j=1}^{169}$ . (b)  $\{t_j^{EV(0)}\}_{j=1}^{169}$ . (c)  $\{t_j^{A(0)}\}_{j=1}^{43}$ .

visual inspection may actually be not anomalies and vice versa. This is because we simply do not have the ground truth to verify what we found. As an example, the experiments shown in Fig. 17, the first seven target pixels were identified by UAC as anomalies but only two pixels in Fig. 20 were actually considered as anomalies by UAC. These two anomalous pixels are indeed rocks hidden in the tree. By visual inspection of Fig. 13(a), there is no way that we knew this fact unless a ground crew was sent to verify what it was exactly the case. So, this experiment provides hard evidence that visual inspection is somewhat subjective and generally cannot be used as a means of determining if a found target pixel is an anomalous pixel. Nevertheless, the greatest advantage of UAC is to offer an objective approach, which automatically determines and classifies anomalies in a set of unlabeled classes with no human manipulations.

Finally, a remark on the data sets used in this paper is noteworthy. As mentioned above, true anomalies can only be identified by ground truth. The TI and TE scenarios and HYDICE provide precise knowledge of targets of interest for verification and validation. Although there are many real data

sets that can be used for experiments, a major issue in using these data sets is no availability of complete ground truth for fact validation. For example, three well-known data sets, Purdue's Indian Pines, Salinas, and University of Pavia [47], have been widely used for hyperspectral image classification but not AD. It is our belief that most anomalies will be in the BKG not the classes provided by ground truth [48]. Since no knowledge is provided about the BKG, there is no way to verify anomaly findings. This may be one of the major reasons that these three scenes have not been used for AD in the literature.

## XI. CONCLUSION

AD has been widely studied in the literature, but how to use AD to perform classification has not been explored. This paper presents a new approach, called *a posteriori* AD, which makes use of *a posteriori* anomaly spatial information obtained directly from processing data to uncover crucial spatial correlation of detected anomalies for UAC. To accomplish this goal, it develops an IAD which takes advantage of a Gaussian filter to obtain spatial correlation surrounding detected anomalies. It then incorporates such Gaussian-filtered spatial information iteratively via feedback loops to update anomaly spatial information. In order to distinguish detected anomalies, it uses ATGP to identify spectrally distinct anomalies among detected anomalies which are further used as desired target signatures for CEM to perform UAC.

The main contributions of this paper can be summarized as follows. First of all, it introduces a new approach, *a posteriori* AD, which uses *a posteriori* anomaly spatial information to perform UAC. Second, it includes IAD in *a posteriori* AD to capture anomaly spatial information. Third, it develops an automatic stopping rule for IAD to determine when the feedback loop should be stopped. This step is crucial because no prior knowledge is available to be used to terminate IAD. Fourth, it uses ATGP or EVs to identify spectrally distinct anomalies from detected anomalies in IAD-detection maps. Fifth, it makes use of CEM in conjunction with Otsu's method to perform UAC. Finally and most importantly, since no prior knowledge is available to determine the number of unlabeled classes, this issue is resolved by implementing IAD coupled with ATGP. To the best of the authors' knowledge, this idea is new and no work is reported on how to determine the number of anomaly classes.

## REFERENCES

- [1] C.-I Chang, *Hyperspectral Imaging: Techniques for Spectral Detection and Classification*. New York, NY, USA: Kluwer, 2003.
- [2] I. S. Reed and X. Yu, "Adaptive multiple-band CFAR detection of an optical pattern with unknown spectral distribution," *IEEE Trans. Acoust., Speech Signal Process.*, vol. 38, no. 10, pp. 1760–1770, Oct. 1990.
- [3] E. A. Ashton and A. Schaum, "Algorithms for the detection of sub-pixel targets in multispectral imagery," *Photogramm. Eng. Remote Sens.*, vol. 64, no. 7, pp. 723–731, Jul. 1998.
- [4] C. M. Stellman, G. G. Hazel, F. Bucholtz, J. V. Michalowicz, A. Stocker, and W. Schaaf, "Real-time hyperspectral detection and cuing," *Opt. Eng.*, vol. 39, no. 7, pp. 1928–1935, Jul. 2000.
- [5] S.-S. Chiang, C.-I Chang, and I. W. Ginsberg, "Unsupervised target detection in hyperspectral images using projection pursuit," *IEEE Trans. Geosci. Remote Sens.*, vol. 39, no. 7, pp. 1380–1391, Jul. 2001.
- [6] D. W. J. Stein, S. G. Beaven, L. E. Hoff, E. M. Winter, A. P. Schaum, and A. D. Stocker, "Anomaly detection from hyperspectral imagery," *IEEE Signal Process. Mag.*, vol. 19, no. 1, pp. 58–69, Jan. 2002.
- [7] D. Manolakis and G. Shaw, "Detection algorithms for hyperspectral imaging applications," *IEEE Signal Process. Mag.*, vol. 19, no. 1, pp. 29–43, Jan. 2002.
- [8] C.-I Chang and S.-S. Chiang, "Anomaly detection and classification for hyperspectral imagery," *IEEE Trans. Geosci. Remote Sens.*, vol. 40, no. 6, pp. 1314–1325, Jun. 2002.
- [9] H. Kwon, S. Z. Der, and N. M. Nasrabadi, "Adaptive anomaly detection using subspace separation for hyperspectral imagery," *Opt. Eng.*, vol. 42, no. 11, pp. 3342–3351, Nov. 2003.
- [10] H. Ren and C.-I Chang, "Automatic spectral target recognition in hyperspectral imagery," *IEEE Trans. Aerosp. Electron. Syst.*, vol. 39, no. 4, pp. 1232–1249, Oct. 2003.
- [11] W. Liu and C.-I Chang, "A nested spatial window-based approach to target detection for hyperspectral imagery," in *Proc. IEEE Int. Geosci. Remote Sens. Symp.*, Anchorage, AK, USA, Sep. 2004, p. 268.
- [12] H. Kwon and N. M. Nasrabadi, "Kernel RX-algorithm: A nonlinear anomaly detector for hyperspectral imagery," *IEEE Trans. Geosci. Remote Sens.*, vol. 43, no. 2, pp. 388–397, Feb. 2005.
- [13] K. I. Ranney and M. Soumekh, "Hyperspectral anomaly detection within the signal subspace," *IEEE Geosci. Remote Sens. Lett.*, vol. 3, no. 3, pp. 312–316, Jul. 2006.
- [14] A. Banerjee, P. Burlina, and C. Diehl, "A support vector method for anomaly detection in hyperspectral imagery," *IEEE Trans. Geosci. Remote Sens.*, vol. 44, no. 8, pp. 2282–2291, Aug. 2006.
- [15] H. Ren, Q. Du, J. Wang, C.-I Chang, J. O. Jensen, and J. L. Jensen, "Automatic target recognition for hyperspectral imagery using high-order statistics," *IEEE Trans. Aerosp. Electron. Syst.*, vol. 42, no. 4, pp. 1372–1385, Oct. 2006.
- [16] C.-I Chang and M. Hsueh, "Characterization of anomaly detection in hyperspectral imagery," *Sensor Rev.*, vol. 26, no. 2, pp. 137–146, 2006.
- [17] H. Goldberg, H. Kwon, and N. M. Nasrabadi, "Kernel eigenspace separation transform for subspace anomaly detection in hyperspectral imagery," *IEEE Geosci. Remote Sens. Lett.*, vol. 4, no. 4, pp. 581–585, Oct. 2007.
- [18] O. Duran and M. Petrou, "A time-efficient method for anomaly detection in hyperspectral images," *IEEE Trans. Geosci. Remote Sens.*, vol. 45, no. 12, pp. 3894–3904, Dec. 2007.
- [19] Y. Tarabalka, T. V. Haavardsholm, I. Kåsen, and T. Skauli, "Real-time anomaly detection in hyperspectral images using multivariate normal mixture models and GPU processing," *J. Real Time Image Process.*, vol. 4, no. 3, pp. 287–300, 2009.
- [20] S. Matteoli, M. Diani, and G. Corsini, "A tutorial overview of anomaly detection in hyperspectral images," *IEEE Aerosp. Electron. Syst. Mag.*, vol. 25, no. 7, pp. 5–28, Jul. 2010.
- [21] H. Kwon and N. M. Nasrabadi, "Kernel RX-algorithm: A nonlinear anomaly detector for hyperspectral imagery," *IEEE Trans. Geosci. Remote Sens.*, vol. 43, no. 2, pp. 388–397, Feb. 2005.
- [22] W. Sakla, A. Chan, J. Ji, and A. Sakla, "An SVDD-based algorithm for target detection in hyperspectral imagery," *IEEE Geosci. Remote Sens. Lett.*, vol. 8, no. 2, pp. 384–388, Mar. 2011.
- [23] B. Du and L. Zhang, "Random-selection-based anomaly detector for hyperspectral imagery," *IEEE Trans. Geosci. Remote Sens.*, vol. 49, no. 5, pp. 1578–1589, May 2011.
- [24] W.-M. Liu and C.-I Chang, "Multiple-window anomaly detection for hyperspectral imagery," *IEEE J. Sel. Topics Appl. Earth Observ. Remote Sens.*, vol. 6, no. 2, pp. 664–668, Apr. 2013.
- [25] J. M. Molero, E. M. Garzón, I. García, and A. Plaza, "Analysis and optimizations of global and local versions of the RX algorithm for anomaly detection in hyperspectral data," *IEEE J. Sel. Topics Appl. Earth Observ. Remote Sens.*, vol. 6, no. 2, pp. 801–814, Apr. 2013.
- [26] S. Khazai, A. Safari, B. Mojarradi, and S. Homayouni, "An approach for subpixel anomaly detection in hyperspectral images," *IEEE J. Sel. Topics Appl. Earth Observ. Remote Sens.*, vol. 6, no. 2, pp. 769–778, Apr. 2013.
- [27] S. Matteoli, T. Veracini, M. Diani, and G. Corsini, "Models and methods for automated background distance estimation in hyperspectral anomaly detection," *IEEE Trans. Geosci. Remote Sens.*, vol. 51, no. 5, pp. 2837–2852, May 2013.
- [28] B. Du and L. Zhang, "A discriminative metric learning based anomaly detection method," *IEEE Trans. Geosci. Remote Sens.*, vol. 52, no. 11, pp. 6844–6857, Nov. 2014.
- [29] S.-Y. Chen, Y. Wang, C.-C. Wu, C. Liu, and C.-I Chang, "Real-time causal processing of anomaly detection for hyperspectral imagery," *IEEE Trans. Aerosp. Electron. Syst.*, vol. 50, no. 2, pp. 1511–1534, Apr. 2014.

- [30] Y. Wang, S.-Y. Chen, C. Liu, and C.-I Chang, "Background suppression issues in anomaly detection for hyperspectral imagery," *Proc. SPIE*, vol. 9124, p. 912413, May 2014.
- [31] S. Nakhostin, H. Clenet, T. Corpetti, and N. Courty, "Joint anomaly detection and spectral unmixing for planetary hyperspectral images," *IEEE Trans. Geosci. Remote Sens.*, vol. 54, no. 12, pp. 6879–6894, Dec. 2016.
- [32] W. Li and Q. Du, "Collaborative representation for hyperspectral anomaly detection," *IEEE Trans. Geosci. Remote Sens.*, vol. 53, no. 3, pp. 1463–1474, Mar. 2015.
- [33] B. Du, R. Zhao, L. Zhang, and L. Zhang, "A spectral-spatial based local summation anomaly detection method for hyperspectral images," *Signal Process.*, vol. 124, pp. 115–131, Jul. 2016.
- [34] B. Du, R. Zhao, L. Zhang, and L. Zhang, "A robust background regression based score estimation algorithm for hyperspectral anomaly detection," *ISPRS J. Photogramm. Remote Sens.*, vol. 122, pp. 126–144, Dec. 2016.
- [35] X. Kang, X. Zhang, S. Li, K. Li, J. Li, and J. A. Benediktsson, "Hyperspectral anomaly detection with attribute and edge-preserving filters," *IEEE Trans. Geosci. Remote Sens.*, vol. 55, no. 10, pp. 5600–5611, Oct. 2017.
- [36] X. Kang, X. Xiang, S. Li, and J. Benediktsson, "PCA-based edge-preserving features for hyperspectral image classification," *IEEE Trans. Geosci. Remote Sens.*, vol. 55, no. 12, pp. 7140–7151, Dec. 2017.
- [37] C.-I Chang, *Real-Time Progressive Hyperspectral Image Processing: Endmember Finding and Anomaly Detection*. New York, NY, USA: Springer, 2016, ch. 15.
- [38] L.-C. Lee, D. Paylor, and C.-I Chang, "Anomaly discrimination and classification for hyperspectral imagery," in *Proc. 7th Workshop Hyperspectral Image Signal Process., Evol. Remote Sens. (WHISPERS)*, Tokyo, Japan, Jun. 2015, pp. 1–4.
- [39] C.-I Chang, *Hyperspectral Data Processing: Algorithm Design and Analysis*. Hoboken, NJ, USA: Wiley, 2013.
- [40] J. C. Harsanyi, "Detection and classification of subpixel spectral signatures in hyperspectral image sequences," Ph.D. dissertation, Dept. Elect. Eng., Univ. Maryland, Baltimore, MD, USA, 1993.
- [41] R. G. Resmini, M. E. Kappus, W. S. Aldrich, J. C. Harsanyi, and M. Anderson, "Mineral mapping with HYperspectral Digital Imagery Collection Experiment (HYDICE) sensor data at Cuprite, Nevada, U.S.A.," *Int. J. Remote Sens.*, vol. 18, no. 17, pp. 1553–1570, 1997.
- [42] C.-I Chang, "Target signature-constrained mixed pixel classification for hyperspectral imagery," *IEEE Trans. Geosci. Remote Sens.*, vol. 40, no. 5, pp. 1065–1081, May 2002.
- [43] N. Otsu, "A threshold selection method from gray-level histograms," *IEEE Trans. Syst., Man, Cybern.*, vol. SMC-9, no. 1, pp. 62–66 Jan. 1979.
- [44] C.-I Chang and Q. Du, "Estimation of number of spectrally distinct signal sources in hyperspectral imagery," *IEEE Trans. Geosci. Remote Sens.*, vol. 42, no. 3, pp. 608–619, Mar. 2004.
- [45] C. C. Wu, C. S. Lo, and C.-I Chang, "Improved process for use of a simplex growing algorithm for endmember extraction," *IEEE Geosci. Remote Sens. Lett.*, vol. 6, no. 3, pp. 523–527, Jul. 2009.
- [46] J. C. Harsanyi and C.-I Chang, "Hyperspectral image classification and dimensionality reduction: An orthogonal subspace projection approach," *IEEE Trans. Geosci. Remote Sens.*, vol. 32, no. 4, pp. 779–785, Jul. 1994.
- [47] *Hyperspectral Remote Sensing Scenes*. [Online]. Available: [http://www.ehu.eus/ccwintco/index.php?title=Hyperspectral\\_Remote\\_Sensing\\_Scenes](http://www.ehu.eus/ccwintco/index.php?title=Hyperspectral_Remote_Sensing_Scenes)
- [48] C.-I Chang, "A review of virtual dimensionality for hyperspectral imagery," *IEEE J. Sel. Topics Appl. Earth Observ. Remote Sens.*, to be published.



**Yulei Wang** received the B.S. and Ph.D. degrees in signal and information processing from Harbin Engineering University, Harbin, China, in 2009 and 2015, respectively.

In 2011, she was awarded by the China Scholarship Council as a joint Ph.D. Student to study in the Remote Sensing Signal and Image Processing Laboratory, University of Maryland Baltimore County, Baltimore, MD, USA. She is currently a Lecturer with the College of Information Science and Technology, Dalian Maritime University, Dalian, China. Her research interests include hyperspectral image processing and vital signs signal processing.



**Li-Chien Lee** received the B.S. degree in electrical engineering from National Taiwan University, Taipei, Taiwan, in 2014, and the M.S. degree in electrical engineering from the University of Maryland Baltimore County, Baltimore, MD, USA, in 2016, where he is currently pursuing the Ph.D. degree with the Remote Sensing Signal and Image Processing Laboratory.

His research interests include hyperspectral imaging, remote sensing, statistical signal processing, machine learning, and large-scale data analysis.



**Bai Xue** (S'15) received the B.E. degree in automation from the Huazhong University of Science and Technology, Wuhan, China, in 2015. He is currently pursuing the Ph.D. degree in electrical engineering with the University of Maryland Baltimore County, Baltimore, MD, USA.

From 2014 to 2015, he was a Program Exchange Undergraduate Student with the Department of Electrical and Computer Engineering, University of Detroit Mercy, Detroit, MI, USA. He is also a Visiting Research Assistant with the Center for in Remote Sensing, Dalian Maritime University, Dalian, China. His research interests include multispectral/hyperspectral imaging, pattern recognition, medical imaging, and medical data analysis.

Hyperspectral Imaging



**Lin Wang** received the B.S. degree in optoelectronic technology and the M.S. degree in physical electronics from Xidian University, Xi'an, China, in 2000 and 2013, respectively.

From 2015 to 2016, she was a Visiting Research Associate Scholar at the Remote Sensing Signal and Image Processing Laboratory, University of Maryland Baltimore County, Baltimore, MD, USA. She is currently an Associate Professor with the School of Physics and Optoelectronic Engineering, Xidian University. Her research interests include hyperspectral image processing, automatic target recognition, and real-time image processing.



**Meiping Song** received the Ph.D. degree from the College of Computer Science and Technology, Harbin Engineering University, Harbin, China, in 2006.

From 2013 to 2014, she was a Visiting Associate Research Scholar at the University of Maryland Baltimore County, Baltimore, MD, USA. She is currently an Associate Professor with the College of Information Science and Technology, Dalian Maritime University, Dalian, China. Her research interests include remote sensing and hyperspectral image processing.



**Chunyan Yu** (M'17) received the B.Sc. and Ph.D. degrees in environment engineering from Dalian Maritime University, Dalian, China, in 2004 and 2012, respectively.

In 2004, she joined the College of Computer Science and Technology, Dalian Maritime University, where she was a Post-Doctoral Fellow with the Information Science and Technology College. From 2014 to 2015, she was a Visiting Scholar with the College of Physicians and Surgeons, Columbia University, New York, NY, USA. She is currently a Lecturer with the Information Science and Technology College, Dalian Maritime University. Her research interests include image segmentation, hyperspectral image classification, and pattern recognition.



**Sen Li** received the B.S. degree in microelectronics from Liao Ning University, Shenyang, China, in 1996, the M.S. degree in information and communication engineering from Dalian Maritime University, Dalian, China, in 1999, and the Ph.D. degree in information and signal processing from the Dalian University of Technology, Dalian, in 2011.

In 2013, she held a post-doctoral position at the Department of Electrical and Computer Engineering, Concordia University, Montreal, QC, Canada. She is currently an Associate Professor with the Department of Information Science and Technology, Dalian Maritime University. Her research interests include array signal processing, communication signal processing, non-Gaussian signal processing, and hyperspectral image processing.



**Chein-I Chang** (S'81–M'87–SM'92–F'10–LF'17) received the B.S. degree in mathematics from Soochow University, Taipei, Taiwan, the M.S. degree in mathematics from the Institute of Mathematics, National Tsing Hua University, Hsinchu, Taiwan, the M.A. degree in mathematics from the State University of New York, Stony Brook, NY, USA, the M.S. and M.S.E.E. degrees from the University of Illinois at Urbana-Champaign, Urbana, IL, USA, and the Ph.D. degree in electrical engineering from the University of Maryland, College Park, MD, USA.

Since 1987, he has been with the University of Maryland Baltimore County, Baltimore, MD, USA, where he is currently a Professor with the Department of Computer Science and Electrical Engineering. From 1994 to 1995, he was a Visiting Research Specialist with the Institute of Information Engineering, National Cheng Kung University, Tainan, Taiwan, where he was also a Distinguished Visiting Fellow/Fellow Professor from 2009 to 2010, both of which were sponsored by the National Science Council in Taiwan. From 2005 to 2006, he was also a Distinguished Lecturer Chair at National Chung Hsing University, Taichung, Taiwan, sponsored by the Ministry of Education in Taiwan, where he was also a Distinguished Chair Professor from 2014 to 2017. He has been holding the Chang Jiang Scholar Chair Professorship and the Director of the Center for Hyperspectral Imaging in Remote Sensing, Dalian Maritime University, Dalian, China, since 2016, the Hua Shan Scholar Chair Professorship with Xidian University, Xi'an, China, since 2016, and a Feng-Tai Chair Professor with the National Yunlin University of Science

and Technology, Douliu, Taiwan, since 2017. He has also been a Chair Professor with Providence University, Taichung, Taiwan, since 2012. He has authored four books, *Hyperspectral Imaging: Techniques for Spectral Detection and Classification* (Kluwer Academic, 2003), *Hyperspectral Data Processing: Algorithm Design and Analysis* (Wiley, 2013), *Real Time Progressive Hyperspectral Image Processing: Endmember Finding and Anomaly Detection* (Springer, 2016), and *Recursive Hyperspectral Sample and Band Processing: Algorithm Architecture and Implementation* (Springer, 2017). He has also edited two books, *Recent Advances in Hyperspectral Signal and Image Processing* in 2006 and *Hyperspectral Data Exploitation: Theory and Applications* (Wiley, 2007), and co-edited with A. Plaza a book on *High Performance Computing in Remote Sensing* (CRC Press, 2007). He holds seven patents on hyperspectral image processing. His research interests include multispectral/hyperspectral image processing, automatic target recognition, and medical imaging.

Dr. Chang is a fellow of the Society for Photo-Optical Instrumentation Engineers (SPIE). He was a recipient of the National Research Council Senior Research Associateship Award from 2002 to 2003, sponsored by the U.S. Army Soldier and Biological Chemical Command, Edgewood Chemical and Biological Center, and Aberdeen Proving Ground, MD, USA. He was a plenary speaker for SPIE Optics + Applications, Remote Sensing Symposium in 2009. He was also a keynote speaker at the User Conference of Hyperspectral Imaging in 2010, Industrial Technology Research Institute, Hsinchu, Taiwan, the 2009 Annual Meeting of the Radiological Society of the Republic of China, Taichung, Taiwan, the 2008 International Symposium on Spectral Sensing Research, and the Conference on Computer Vision, Graphics, and Image Processing in 2003 (Kimen) and 2013, Nan-Tou, Taiwan. He was the Guest Editor of a special issue of the *Journal of High Speed Networks on Telemedicine and Applications* in 2000, and a Co-Guest Editor of another special issue of the same journal on *Broadband Multimedia Sensor Networks in Healthcare Applications* in 2007. He was also the Co-Guest Editor of special issues on *High Performance Computing of Hyperspectral Imaging* for the *International Journal of High Performance Computing Applications* in 2007, *Signal Processing and System Design in Health Care Applications* for the *EURASIP Journal on Advances in Signal Processing* in 2009, and *Multippectral, Hyperspectral, and Polarimetric Imaging Technology* for the *Journal of Sensors and Hyperspectral Imaging and Applications for Remote Sensing* in 2017. He was an Associate Editor of *Hyperspectral Signal Processing* for the *IEEE TRANSACTIONS ON GEOSCIENCE AND REMOTE SENSING* from 2001 to 2007. He is currently an Associate Editor of the *Artificial Intelligence Research* and also on the editorial boards of the *Journal of High Speed Networks*, *Recent Patents on Mechanical Engineering*, the *International Journal of Computational Sciences and Engineering*, the *Journal of Robotics and Artificial Intelligence*, and the *Open Remote Sensing Journal*.